Title: BRD4-mediated epigenetic regulation of endoplasmic reticulum-mitochondria contact sites is governed by the mitochondrial complex III

Authors: Brandon Chen[1,2], Theophilus M. Lynn-Nguyen[2,3,16], Pankaj Jadhav[5,6], Benjamin S. Halligan[2,3] , Nicholas J. Rossiter[1,2], Rachel M. Guerra[7], Sergei Koshkin[8], Imhoi Koo[8], Pietro Morlacchi[9], David A. Hanna[10], Jason Lin[2], Ruma Banerjee[10], David J. Pagliarini[7,11,12], Andrew D. Patterson[8], Shyamal Mosalaganti[5,6,13], Jonathan Z. Sexton[2,3,14,15,16], Tito Calì[17,18,19], Costas A. Lyssiotis[1,2,4,20,*], Yatrik M. Shah[1,2,4,20,*]

[1]Cellular and Molecular Biology Program, University of Michigan Medical School, Ann Arbor, MI 48109, USA
[2]Department of Molecular & Integrative Physiology, University of Michigan, Ann Arbor, MI 48109, USA.
[3]Department of Medicinal Chemistry, College of Pharmacy, University of Michigan, Ann Arbor, MI 48109
[4]Department of Internal Medicine, Division of Gastroenterology and Hepatology, Michigan Medicine at the University of Michigan, Ann Arbor, MI 48109
[5]Life Sciences Institute, University of Michigan, Ann Arbor, Michigan, 48109, United States.
6 Department of Cell and Developmental Biology, University of Michigan, Ann Arbor, Michigan, 48109, United States.
[7]Department of Cell Biology and Physiology, Washington University School of Medicine, St. Louis, MO 63110, USA
[8]Department of Veterinary and Biomedical Sciences, The Pennsylvania State University, University Park, PA, USA
[9]Agilent Technologies, Inc., Lexington, MA, 02421, USA
[10]Department of Biological Chemistry, University of Michigan Medical School, Ann Arbor, MI, 48109, USA
[11]Department of Biochemistry and Molecular Biophysics, Washington University School of Medicine, St. Louis, MO ,63110, USA
[12]Departament of Genetics, Washington University School of Medicine, St. Louis, MO, 63110, USA
[13]Department of Biophysics, College of Literature, Science and the Arts, University of Michigan, Ann Arbor, MI, 48109, United States.
[14]Center for Drug Repurposing, University of Michigan, Ann Arbor, MI, 48109, USA
[15]Michigan Institute for Clinical and Health Research, University of Michigan, Ann Arbor, MI 48109, USA
[16]College of Pharmacy, University of Michigan, Ann Arbor, MI, 48109, USA
[17]Department of Biomedical Sciences, University of Padova, 35131, Padova, Italy
[18]Padova Neuroscience Center (PNC), University of Padova, 35131, Padova, Italy
[19]Center for Neurodegenerative Disease Research (CESNE), University of Padova, 35131, Padova, Italy
[20]Rogel Cancer Center, University of Michigan, Ann Arbor, MI, USA
* To whom correspondence should be addressed: shahy@umich.edu, clyssiot@umich.edu

Keywords: Endoplasmic reticulum-mitochondria contact sites, bromodomain protein, high-throughput screening, mitochondrial electron transport chain.

Abstract:

Inter-organellar communication is critical for cellular metabolic homeostasis. One of the most abundant inter-organellar interactions are those at the endoplasmic reticulum and mitochondria contact sites (ERMCS). However, a detailed understanding of the mechanisms governing ERMCS regulation and their roles in cellular metabolism are limited by a lack of tools that permit temporal induction and reversal. Through unbiased screening approaches, we identified fedratinib, an FDA-approved drug, that dramatically increases ERMCS abundance by inhibiting the epigenetic modifier BRD4. Fedratinib rapidly and reversibly modulates mitochondrial and ER morphology and alters metabolic homeostasis. Moreover, ERMCS modulation depends on mitochondria electron transport chain complex III function. Comparison of fedratinib activity to other reported inducers of ERMCS revealed common mechanisms of induction and function, providing clarity and union to a growing body of experimental observations. In total, our results uncovered a novel epigenetic signaling pathway and an endogenous metabolic regulator that connects ERMCS and cellular metabolism.

Main Texts:

The dynamic regulation of organelle networks and inter-organellar communication is critical for cellular metabolism and physiology. Inter-organellar communication occurs at membrane contact sites, which directly regulate metabolite transport, protein complex organization, signaling and organellar function[1,2]. One of the most well studied and abundant inter-organellar contact sites are endoplasmic reticulum-mitochondria contact sites (ERMCS). While a wealth of research has defined the unique proteome at ERMCS, the precise spatiotemporal regulation by various signaling pathways, and evolutionarily conserved molecular tethering complexes that structurally support ER-to-mitochondria interactions remains still elusive. Functional genetic and biochemical studies have revealed essential roles of ERMCS, including phospholipid synthesis[3], calcium buffering[4], mitochondrial dynamics[5,6], mitochondrial DNA distribution[7] and autophagosome formation[8].

Dysregulation of ERMCS and tethers contributes to the etiology of various disease, including neurodegeneration[9], obesity[10], cancer[11], diabetes[12], and inborn errors of metabolism[13]. Understanding the fundamental mechanisms underlying ERMCS dysregulation is essential for identifying potential drug targets to restore ERMCS function in disease. However, significant gaps persist in our basic understanding of the molecular drivers governing the remodeling and organization of ERMCS. Moreover, the exact mechanisms by which the microenvironment, signal transduction, and molecular cues initiate, maintain, and modify adaptive responses of ERMCS are yet to be fully elucidated.

In this study, we have identified a novel epigenetic response and a metabolic redox state that regulate the formation and dynamics of ERMCS. We characterized an FDA-approved compound, fedratinib, which induces ERMCS formation via BRD4-mediated histone recognition and described it as a new tool for temporal, reversible control of ERMCS. Fedratinib treatment establishes selective ER wrapping around mitochondria with cristae structure defects, membrane potential loss, and metabolic rewiring. ERMCS induction requires an intact mitochondrial complex III, which is a major site of coenzyme Q (CoQ) oxidation. Attempts to modulate mitochondrial CoQ redox state suggest a potential mechanism where an increase in the reduced-to-oxidized CoQ ratio could block ERMCS. Importantly, our study demonstrates that the transcriptional and metabolic requirements for ERMCS induction by fedratinib are common to other cellular stressors known to triggers ERMCS and underscores the existence of a conserved regulatory network governing ERMCS.

High throughput pharmacogenomic screening identifies novel regulators of ERMCS. To follow ERMCS in living cells in real-time, we generated a panel of eleven isogenic gene-edited cell lines with a novel reversible split fluorescent ERMCS reporter, termed split-GFP based

contact site sensor (SPLICS) [14–16]. This genetically encoded sensor is stably integrated with a doxycycline-inducible promoter for titrating reporter expression[17]. In addition, we engineered a mitochondria matrix reporter (mitoTagRFP) to control for gene expression and monitor mitochondrial abundance[18] (Fig. 1a). Single cell clones were profiled for those with inducible and reversible green fluorescence as well as stable red fluorescence. Probe induction did not have a deleterious effect on cell growth for at least 72 hours after reporter induction. To demonstrate the sensitivity, accuracy, and specificity of the probe, SPLICS lines were treated with a known inducer of ERMCS, the ER stress inducer thapsigargin[19] (Fig 1b), or by over-expressing an artificial ER-mitochondria linker (ER-MT tether). Both treatments increased the SPLICS signal significantly (Fig. 1c).

To discover novel mediators and chemical tools of ERMCS induction, we developed a high-content phenotypic imaging screen with machine learning categorization approaches using our SPLICS lines and assayed an FDA-approved drug repurposing library (Fig. 1d). Consistent with known roles of ER stress in ERMCS, we identified proteasome inhibitors bortezomib and carfilzomib[20]. Moreover, we identified microtubule inhibitors that modulate organelle movement within in cells[21] (Supplementary Table 1). We decided to focus on fedratinib as it induced high levels of ERMCS, and its annotated mechanisms of action have not been associated with ERMCS regulation (Fig. 1d). Fedratinib inhibits Janus kinase 2 (JAK2) as well as bromodomain-containing protein 4 (BRD4)[22]. The increase in ERMCS following fedratinib treatment was observed in a large panel of human and mouse cell lines (Fig 1e and Supplementary Table 2). We focused on SW480 and HT1080, as these had the highest fold change by fedratinib. ERMCS induced by fedratinib is both dose- and time-dependent with estimated ED_{50} and ET_{50} values of 666.8 nM/4.7hr (SW480) and 404.7 nM/7.8 hr (HT1080, which was evident using both the SPLICS reporter lines as well as by an orthogonal method that measures ERMCS (Fig. 1f and g; Extended Movies 1 and 2; Extended Data Fig. 1a). Importantly, the increase in ERMCS is reversible following a washout of fedratinib from the culture media, and highlighting the capability of SPLICS reporters to dynamically and reversibly measure organelle contact sites in living cells (Fig. 1h). Collectively, this screen identified the first FDA-approved drug with potent bioactivity in increasing ERMCS across cell lines with distinct tissue and organisms of origin.

Bromodomain and Extra-Terminal protein (BET)-dependent transcription response is required for ERMCS induction. Fedratinib was first described as a JAK2-specific inhibitor for treating myelodysplastic syndromes[23]. Thus, we tested the ERMCS-inducing activity of other JAK2 inhibitors. We found that the JAK2 inhibitor Ruxolitinib did not induce ERMCS formation at a concentration that inhibits JAK2-dependent STAT3 phosphorylation (Fig. 2a and Extended Data Fig. 2a). Fedratinib has other targets, including BRD4, a member of the bromodomain and extra-terminal (BET) epigenetic reader family[24–26]. Fedratinib binds to the acetylated-lysine recognition pocket of BRD4 and prevents BRD4 interaction with acetylated histones. Indeed, we observed that canonical BRD4-hypersensitive targets, such as c-MYC, were decreased in expression upon fedratinib treatment (Extended Data Fig. 2b). Similar to fedratinib, other inhibitors of BRD4 from our small molecule screen also increased ERMCS (i.e. OTX-015 and IBET-762; Zenodo DOI: 10.5281/zenodo.10214159). To directly assess BRD4, we utilized the PROTAC degrader of BRD4, dBET6, and siRNA-mediated knockdown (KD), both of which increased ERMCS (Fig. 2a and b; Extended Data Fig. 2a).

To identify whether BRD4-dependent ERMCS induction is transcriptionally regulated, we inhibited transcription kinases cyclin-dependent kinases 8 and 9 (CDK8 and CDK9). Inhibition of CDK8 and CDK9 both suppressed ERMCS induction (Fig. 2C and Extended Data Fig. 2c), thus pointing out the importance of an active transcriptional program for ERMCS regulation. To further test this we performed a pulse-chase experiment with RNA polymerase II (RNA pol II) inhibitor Actinomycin D (ActD) was performed. Fedratinib- and thapsigargin-induced ERMCS

were suppressed when transcription activity was rapidly blocked (Extended Data Fig. 2d and e), whereas the mitochondrial RFP signal was stable following acute transcriptional blockade.

To characterize the early transcriptional response upon ERMCS induction, we conducted nascent mRNA sequencing, BrU-Seq, 2hr after fedratinib treatment. We identified potent upregulation of genes associated with the integrated stress response (ISR) and the unfolded protein response (UPR) (Fig. 2d; Extended Data Fig. 2h and Supplementary Table 3). Two canonical ISR markers, ATF4 and phosphorylated-eIF2α at Ser51, were validated by western blot (Extended Data Fig. 2f). Although thapsigargin is thought to increases ERMCS via inducing ER stress, fedratinib does not increase the UPR markers CHOP and BiP (Extended Data Fig. 2g). We, therefore, posit that fedratinib and thapsigargin potentially induce ERMCS via the upregulating the ISR.

To identify the BRD4 co-regulated complex and transcription factors that coordinate ERMCS modulation, we performed an unbiased CRISPR screen coupled with fluorescent activated cell sorting (FACS), using a nuclear genome library. Following transduction with the CRISPR library, which contained genes annotated with nuclear localization or roles in epigenetic modification. Following transduction with the CRISPR library, we induced ERMCS formation with fedratinib, and sorted cells that failed to induce ERMCS (SPLICS^{low}/mitoTagRFP) (Fig. 2e). Through gene set enrichment analyses (GSEA), we found a potent signature from components of the mediator complex (Fig. 2f and g; Supplementary Table 4). The mediator complex is a hetero-multimeric protein complex that recruits other transcription factors, co-regulators, and RNA pol II machineries along with BRD4. We generated knowkcdowns of mediator complex components MED16 and MED24 KD via CRISPR interference (CRISPRi), which failed to induce ERMCS in response to fedratinib or thapsigargin (Fig. 2h and Extended Data Fig. 2i).

Taken together, here we have demonstrated that Fedratinib induces ERMCS via suppression of BRD4, and this activity is transcriptionally controlled. Moreover, induction of ERMCS via the ER stressor thapsigargin also depends on an active gene expression program, indicating that transcriptional rewiring to be common for other modes of ERMCS induction.

Fedratinib induces novel ultrastructural changes at ERMCS and heterogenous mitochondrial morphology and function. Organelle structures and inter-organellar organization networks inform the metabolic state of cells. An increase in ERMCS drives adaptive oxidative phosphorylation and supports ER homeostasis. Therefore, we postulate that understanding how fedratinib impacts ERMCS architecture will provide valuable information for a deeper understanding of the metabolic factors, regulation, and consequences of ERMCS induction. We conducted transmission electron microscopy on SW480 and HT1080 cells. We observed structural changes, such as the ER membrane enveloping the mitochondria and the collapse of cristae, we also noted the compartmentalization of structures within the inner mitochondrial membrane (IMM) (Fig. 3a). In addition, approximately 15-20% of mitochondria exhibited complete loss cristae and 40-45% demonstrated compartmentalization of the IMM (Fig. 3a). Although we did not observe consistent changes in circular cross-section, area, or aspect ratio, a higher variability of these structural indices were seen in fedratinib-treated cells (Extended Data Fig. 3a-d). Next, we performed correlative light and electron microscopy (CLEM) analysis to visualize contact site morphology at a better spatial resolution. With the SPLICS reporter as a convenient fluorescence marker for ERMCS, we used electron tomography (ET) at ERMCS to generate a three-dimensional volume of ERMCS in SW480 cells (Fig. 3b). Fedratinib treated cells, but not vehicle controls, exhibit direct ER and outer mitochondrial membrane (OMM) juxtaposition at selective SPLICS$^{positive\ (+)}$ locations (Fig. 3c). Moreover, inner mitochondrial membrane/cristae exhibit near complete collapse at contact sites. ERMCS are typically characterized by segments of the ER membrane contacting the outer mitochondrial membrane (OMM)[27], rather than the ER membrane enveloping entire mitochondria, as observed following fedratinib treatment. In other words, fedratinib-treatment not only leads to

classic features of ERMCS, but it also promotes a novel ultrastructural re-organization at ERMCS.

Intact mitochondria and ER networks, dynamics, and morphology in the whole cell were imaged with light microscopy. We found that a subset of mitochondria was rounded and swollen in fedratinib treated cells, and colocalized with the ERMCS SPLICS reporter sites, suggesting that the very close proximity with the ER is needed to promote the above-mentioned ultrastructural re-organization of mitochondria. Meanwhile, SPLICS^{negative} mitochondria with a higher ERMCS distance still form normal network-like morphology. However, OMM proteins (MFN2, DRP1, and phospho-DRP1$^{S616/637}$), IMM organization proteins (OPA1, MICOS complex component MIC60 and MIC25), and mitochondrial electron transport chain (ETC) expression did not change in whole cell western blots (Extended Data Fig. 4a and b). In addition, expression of the ER sheet and tubule shaping proteins CLIMP63 (CKAP4) and RTN4 did not change (Extended Data Fig. 4c). These data suggest that the structural changes of ERMCS induction by fedratinib did not induce changes by altering levels of the canonical mitochondria dynamics or ER structure shaping proteins. However, we cannot rule out local signaling events that could alter organellar structures at specific ERMCS foci.

To further characterize the mitochondria, we profiled mitochondrial mass, membrane potential (MMP/ΔΨm), oxygen consumption rate (OCR), extracellular acidification rate (ECAR), mitochondria reactive oxygen species (ROS), mitochondrial calcium response, and mitochondrial DNA (mtDNA) content. Again, we did not observe consistent differences between fedratinib versus control-treated cells in bulk measurements from whole cells (Extended Data Fig. 4d-k). Since these mitochondrial phenotyping approaches report changes in the average behavior at a whole cell level changes, they could mask phenotypic differences since not all mitochondria are wrapped by ER in fedratinib-treated cells. Rather, the majority of mitochondria continue to exhibit normal morphology.

These points notwithstanding, we investigated the impact of fedratinib on whole cell metabolism using metabolomics and lipidomics. Through dimensional reduction approaches to identify variability in metabolite and lipid profiles, we found that the metabolome is significantly altered upon induction of ERMCS (Fig. 3d; Extended Data Fig. 5a-c; Supplementary Table 5). Indeed, the changes to the lipidome were even more profound when we performed lipidomics on mitochondria isolated from fedratinib treated cells. Compared to the whole cell and ER/microsome fractions, we observed a dramatic decrease in mitochondrial lipids (Fig. 3e). Since loss of cardiolipin, a mitochondrial inner membrane lipid, or alteration in the phospholipid saturation state can directly affect cristae organization[28]. With these data in mind, we next employed single mitochondria functional profiling with fluorescence imaging, which revealed intra-cellular heterogeneity in mitochondria membrane potential. Mitochondria wrapped with ER (SPLICS^{+}) have lower ΔΨm compared to those lacking ERMCS (Fig. 3f-h; Extended Data Fig. 6b). Orthogonal validation with single mitochondria flow cytometry further confirmed lower ΔΨm when ERMCS is induced that is absent at the whole cell level (Fig. 3i). Of note, we did not observe changes in mitochondrial ROS at the single mitochondrial level (Extended Data Fig. 6a and c).

ETC Complex III function is necessary for ERMCS formation. Based on the drastic mitochondrial structural and less pronounced but significant metabolic changes associated with ERMCS induction, we hypothesized that an optimal metabolic state would be required to sustain metabolic demands for ERMCS formation. To test this model, we employed a variety of mitochondrial perturbations, and found that hypoxia suppresses ERMCS (Fig. 4a). In addition to directly inhibiting oxygen dependent-reactions[29], hypoxia also rewires cellular metabolism through hypoxia inducible factors (HIFs). In contrast to hypoxia, HIF induction with the PDH inhibitor FG-4592 did not similarly attenuate fedratinib-induced ERMCS, indicating that the hypoxia effect is independent of HIF activation but oxygen dependent (Fig. 4a).

Since mitochondria are the largest oxygen consumers within the cell, we inhibited the individual electron transport chain (ETC) complexes I-V, or depolarized membrane potential, and then asked whether a specific ETC component is required for ERMCS induction (Fig. 4b). Only complex III and IV inhibition suppressed the formation of ERMCS induced by fedratinib (Fig. 4c). Unlike ETC inhibitors that restrict oxygen consumption and generate mitochondrial ROS, inhibiting complex III or IV suppresses the ability to carry out CoQ/ubiquinol oxidation Inhibition of complex III and IV leads to the buildup of $CoQH_2$, thus increasing the $CoQH_2$/CoQ ratio, which has been associated with reverse electron transport (RET) at complex I and II, generating ROS and reducing fumarate to succinate[30], respectively.

We found that treatment with neither the mitochondrial-specific ROS inducer mito-paraquat (mitoPQ) nor a complex I inhibitor that increases the proportion of oxidized CoQ suppressed ERMCS formation (Extended Data Fig. 7a). Therefore, we hypothesized that complex III inhibition could suppress ERMCS formation from accumulation of reduced $CoQH_2$. To relieve $CoQH_2$ buildup, we genetically expressed a *Ciona intestinalis* alternative oxidase (AOX)[30], which oxidizes $CoQH_2$ to CoQ in an antimycin/myxothiazol-insensitive manner (Fig. 4d). If $CoQH_2$ accumulation drives ERMCS suppression, AOX expression should restore ERMCS induction by maintaining an oxidized CoQ pool. Notably, cells expressing AOX retain fedratinib-induced ERMCS when simultaneously subjected to complex III inhibitors (Fig. 4e; Extended Data Fig. 7b). This regulation is not limited to fedratinib as thapsigargin induced ERMCS are also regulated by similar mechanisms (Extended Data Fig. 7c and d). Surprisingly, fedratinib did not directly alter the $CoQH_2$/CoQ redox ratio or CoQ_{10} abundance at the whole cell or mitochondria level (Extended Data Fig. 7e and f). This suggest that perhaps maintaining the ability for complex III to carry out CoQ oxidation, rather than the total levels, is crucial for ERMCS induction.

In addition to expressing AOX, we also utilized an orthogonal method to alter electron flow to complex III. Under standard conditions, complex I contributes the majority of electrons to the ETC via NADH. Co-inhibiting complex I and complex III limits $CoQH_2$ generation, thereby decreasing the $CoQH_2$/CoQ ratio. Indeed, inhibition of complex I and III restored ERMCS inducibility (Fig. 4f). We attempted to rescue the impact of complex IV inhibitors, H_2S and hypoxia, by similarly inhibiting complex I. However, piericidin A was unable to restore ERMCS levels (Extended Data Fig. 7g and h). This may be attributed to the dominant role of SQOR-mediated CoQ reduction as the main electron donor under H_2S conditions, as well as the inhibition of NADH-dependent electron flux into the ETC during hypoxia.

These findings support that complex III-dependent functions such as CoQ oxidation could influence the dynamic induction of ERMCS formation. More importantly, this regulation is not limited to fedratinib induced ERMCS, as ERMCS induced by thapsigargin also responds to methods that bypass Complex III or CoQ oxidation state manipulation. Consequently, we can conclude that the Complex III regulated CoQ oxidation could act as a reliable indicator of ERMCS dynamics and is a novel metabolic pre-requisite for ERMCS induction.

Discussion:

Inter-organellar contact sites mediate local signaling events, whole cell metabolism and tissue physiology. The dysregulation of ERMCS has been implicated in diseases including cancer, fragile X syndrome[31], and Friedrich's ataxia[13]. Despite their critical role in maintaining metabolic homeostasis, the mechanisms governing the dynamics of ERMCS remain elusive (*28*), at least in part due to the lack of potent inducers with temporal control. We identified fedratinib, an FDA-approved drug for myelodysplastic syndrome that robustly induced the formation of ERMCS across diverse cell lines. We demonstrated that the relevant molecular target of fedratinib was the epigenetic regulator BRD4, and inhibition initiated an activating gene expression program that coordinated with mediator complex to induce ERMCS. The ERMCS observed in response to fedratinib exhibited novel ultrastructural changes including a tight

wrapping of the ER membrane that envelopes the entire mitochondrial membrane at a subset of mitochondria in the mitochondrial network.

Despite these structural alterations, no consistent changes were observed in various ER and mitochondrial functions at the whole-cell level. We found this to be remarkable, given that upwards of 30% of mitochondria exhibited massive structural alternations, indicating that "normal" mitochondria may compensate to support cell homeostasis when other mitochondria are dysfunctional. In either case, this underscores the significance of considering mitochondrial heterogeneity in the study of ERMCS. Moreover, through probing ETC functions, we demonstrated that ERMCS depends on mitochondria complex III/IV activities, and methods bypassing their functions could restore ERMCS abundance. This suggests that non-affected mitochondria adapt or persist when complex III function is suppressed, whereas the affected mitochondria are targeted for ER engulfment.

Previous studies of BRD4 predominantly focused on its ability to act as a positive regulator of transcription[32]. In contrast, our findings demonstrate that de-repression of its target gene expression is required for ERMCS activity. Inhibition of BRD4 activates autophagy-related genes and corrects for mitochondrial disease phenotype by increasing mitochondrial biogenesis program[33,34]. However, the direct transcriptional target(s) of BRD4 that regulate ERMCS are not clear. Through transcriptomics we identified activation of the ISR in both cells with high basal ERMCS and following fedratinib treatment. ISR activation relies on inducing PERK, HRI, GCN2, and PKR[35]. Recent work has demonstrated that mitochondrial stress and sublethal activation of mitochondrial outer membrane permeabilization (MOMP) can release cytochrome c and subsequently activate ISR[36]. Interestingly, the loss of cristae at ERMCS resembles the effect induced by MOMP activation[37]. Moreover, the dynamic nature of ERMCS are involved in apoptosis regulation and sensitivity[38,39]. Clearly many compelling connections exist between ISR signaling and the regulation of ERMCS, and discerning the relationship between ISR and ERMCS warrants further study.

The ratio of oxidized CoQ to reduced $CoQH_2$ plays a critical signaling role that reflects cellular metabolic states. While recognized as an electron carrier in the ETC [40], CoQ has emerged as a multifunctional lipid involved in ferroptosis[41,42], pyrimidine biosynthesis[43], H_2S detoxification[44], glycerol phosphate shuttle, and proline catabolism[45]. Accumulation of $CoQH_2$ under hypoxia or sulfide exposure is essential to maintain tissue homeostasis by utilizing fumarate as a terminal electron acceptor instead of oxygen[30,44]. In physiological or pathological hypoxia, tissues rewire metabolism via the canonical HIF oxygen sensing pathway and reorganize organellar networks to maintain metabolism and other aspects of cellular homeostasis. Indeed, we demonstrated that ETC complex III and IV could sustain a critical function needed for establishing ERMCS as inhibiting complex III and IV inhibited ERMCS. Utilizing genetic methods to bypass complex III inhibition via ectopic expression of alternative oxidase (AOX) restored ERMCS abundance under complex III inhibition. Surprisingly, limiting electron entry from complex I reversed the inhibitory response of antimycin or myxothiazol and re-activated ERMCS induction. Based on the AOX and complex I/III co-inhibition results, we speculate that there could potentially be a CoQ redox sensing mechanism as both rescue approaches should prevent $CoQH_2$ accumulation under complex III inhibition alone. Further studies to profile CoQ oxidation state on the subcellular level and spatial distribution will be critical for drawing definitive conclusions with the inconsistent change in CoQ redox state and CoQ abundance. Thus, we provide evidence to support that modulation of oxygen tension re-organizes the subcellular organellar landscape and Complex III function could potentially be an endogenous metabolic sensor for ERMCS formation. Importantly, while we made this discovery with fedratinib, we also illustrated that other ERMCS inducers, like the ER stressor thapsigargin, require the same molecular and metabolic mechanisms for ERMCS. This evidence suggests the mechanisms described here are broadly applicable to other ERMCS regulatory modalities.

In conclusion, our study underscores the intricate interplay between molecular regulators and metabolic cues that dictate the formation and functionality of ERMCS. Moreover, we characterize a tool compound that can temporally and reversibly modulate ERMCS laying the foundation for potential therapeutics targeting inter-organellar communication in diverse disease contexts.

Materials and Methods:

Cell culture: HT1080, SW480 HCT116, DLD1, SW480, HeLa, U2OS, A459, PA-TU8902, K562, Jurkat, B16, KPC7940 cells were maintained at 37°C in 5% CO_2 and 21% O_2. HT1080, SW480 HCT116, DLD1, SW480, HeLa, U2OS, A459, PA-TU8902, B16, and KPC7940 cells were cultured in Dulbecco's Modified Eagle Medium (DMEM) supplemented with 10% FBS and 1% antibiotic/antimycotic, whereas Jurkat and K562 cells were cultured in Roswell Park Memorial Institute (RPMI) supplemented with 10% FBS and 1% antibiotic/antimycotic.

Generation of SPLICS stable cell lines: The SPLICS reporter is composed of a split GFP_{1-10} barrel localized to the mitochondrial outer membrane, a P2A self-cleavage signal for equimolar expression, and the remaining $beta_{11}$ fragment targeted to the ER membrane. Upon ERMCS formation within the 8-10 nm distance, the split-GFP reporter forms intact GFP. Doxycycline-inducible SPLICS reporter stable cell lines were generated via a three-plasmid PiggyBac transposase system. Cells were co-transfected with the plasmids using Lipofectamine 2000 transfection reagent, then the next day selected with 2 mg/ml of G418 (Geneticin) for 7 days. After selection, 100 ng/ml of doxycycline were used to induce reporter expression, and GFP positive cells were sorted on Bigfoot Spectral Cell Sorter (Invitrogen) to isolate GFP positive clones. Clones were cultured and screened for accurate localization of SPLICS reporter to mitochondria and ER via live cell imaging and for normal mitochondrial oxygen consumption rate. For ERMCS analysis with SPLICS, cells will be induced with 100 ng/ml of doxycycline for minimally 24 hr before treatment or analysis.

Generation of knockout and overexpression cell lines: sgRNAs (oligonucleotide sequences are indicated in Supplementary Table 5) were ligated into BsmBI-linearized lentiCRISPR-v2 (for CRISPR KO) or pLV hU6-sgRNA hUbC-dCas9-KRAB-T2a-Puro (pLV hU6-sgRNA hUbC-dCas9-KRAB-T2a-Puro was a gift from Charles Gersbach (Addgene plasmid # 71236; http://n2t.net/addgene:71236 ; RRID:Addgene_71236)) with T4 ligase (NEB). AOX overexpression plasmid was achieved with pCW57.1_AOX-FLAG (pCW57.1_AOX-FLAG was a gift from David Sabatini & Jessica Spinelli (Addgene plasmid # 177984; http://n2t.net/addgene:177984 ; RRID:Addgene_177984)). MitoTagRFP plasmid was acquired from Addgene (pclbw-mitoTagRFP was a gift from David Chan (Addgene plasmid # 58425; http://n2t.net/addgene:58425 ; RRID:Addgene_58425). BFP and BFP-ER-mitochondria tether were generated via Vectorbuilder (pLV[Exp]-Bsd-CMV>{new mTagBFP2} and pLV[Exp]-Bsd-CMV>{new mTagBFP2 ER mito tether}). Lentiviral vectors expressing sgRNAs were transfected into HEK293T cells with lentiviral packaging vectors CMV VSV-G and psPAX2 using XtremeGene 9 transfection reagent (Roche). After 24 h, media was aspirated and replaced by fresh media. The virus-containing supernatant was collected 48 h after transfection and filtered using a 0.45 mm filter to eliminate cells. Cells to be transduced were plated in 6-well tissue culture plates and infected in media containing virus and 8 µg/mL of polybrene. Cells were spin infected by centrifugation at 1,100 g for 1.5 h. After transduction, media was changed, and cells were selected with puromycin (for sgRNA lentiviral vector) for 72 hrs.

siRNA mediated knockdown: siRNAs for BRD4 were transfected using a reverse transfection protocol and Lipofectamine RNAiMAX. siRNA was purchased from Horizon Discovery with the following information: siGENOME Human BRD4 (23476) siRNA - SMARTpool, 5 nmol.

Western Blots: Whole-cell lysate preparations were described previously (Anderson et al., 2013). Whole cell lysates were prepared from cell lines by RIPA buffer. Homogenates were incubated in RIPA buffer for 15 min on ice followed by 13,000 rpm centrifugation for 15 min. Supernatants were transferred to a new tube and mixed with 5× Laemmli buffer and boiled for 5 min. Lysates containing 30–40 µg of protein per well were separated by SDS-PAGE, transferred onto nitrocellulose membranes, and immunoblotted overnight at 4°C with indicated antibodies. All the primary antibodies were used at a dilution of 1:1000. HRP-conjugated secondary antibodies used were anti-rabbit and anti-mouse at a dilution of 1: 2000 and immunoblots were developed using the iBright Imaging System and iBright Analysis Software (Thermofisher).

Antigen	**Company**	**Catalog number**
Vinculin (clone: E1E9V)	Cell Signaling Technology	13901
MFN2 (clone: D2D10)	Cell Signaling Technology	9482
DRP1 (clone: D6C7)	Cell Signaling Technology	8570
pS616-DRP1	Cell Signaling Technology	3455
pS637-DRP1	Cell Signaling Technology	4867
Mitofilin/MIC60/IMMT	Proteintech	10179-1-AP
MIC25/CHCHD6	Proteintech	20639-1-AP
RTN4/NOGO	Proteintech	10740-1-AP
CLIMP63/CKAP4 (clone: G1/296)	Enzo Life Science	ENZ-ABS669-0100
OPA1 (clone: D6U6N)	Cell Signaling Technology	80471
ATF4 (clone: E4Q4E)	Cell Signaling Technology	97038
BiP/HSPA5 (clone: C50B12)	Cell Signaling Technology	3177
CHOP/DDIT3 (clone: L63F7)	Cell Signaling Technology	2895
BRD4 (clone: E2A7X)	Cell Signaling Technology	13440
c-MYC (clone: E5Q6W)	Cell Signaling Technology	18583
STAT3 (clone: 123H6)	Cell Signaling Technology	9139
pY705-STAT3 (clone: D3A7)	Cell Signaling Technology	9145
IP3R-I/II/III (clone: B-2)	Santa Cruz Biotechnology	SC-377518
VDAC1/Porin + VDAC3 (clone: 20B12AF2)	Abcam	Ab13734

CRISPR Screen: For the epigenetics library screen in SW480 reporter cells, the human sgRNA library was described in this paper[46] was used. The titer of lentiviral supernatants was determined by infecting targets cells at several amounts of virus in the presence of polybrene (10 ug/mL), counting the number of drug resistant infected cells after 3 days of selection. 40 million target cells were infected at an MOI of ~0.5 and selected with puromycin (1 ug/mL) 72 h after infection. An initial pool of 30 million cells was harvested for genomic DNA extraction. The remaining cells were cultured for 6 days, treated with fedratinib for 24 hr, then 25 million cells were sorted from the top and bottom 20% of SPLICS/mitoTagRFP fluorescent ratio on day 8. After which cells were harvested for genomic DNA extraction. sgRNA inserts were PCR amplified (primers listed in Supplementary Table 5, purified and sequenced on a NextSeq (Illumina). Sequencing reads were mapped and the abundance of each sgRNA was tallied. Gene score is defined as the median log2 fold change in the abundance between the initial and final population of all sgRNAs targeting that gene. Full result of the screen with sequencing primers can be found in the supplemental data.

CRISPR screen analysis: sgRNA read counts were generated by aligning sequencing reads to the sgRNA library sequences, with only exact matches allowed. sgRNA abundances were calculated for both sorted populations by first adding a pseudocount of 1, then dividing by the total number of reads in each given sample. For each sgRNA, a differential score was calculated as the log2 fold-change in sgRNA abundance between the GFP-high and GFP-low cell populations. Gene level differential scores were generated by taking the mean score of all sgRNAs targeting the same gene. The set of differential gene scores was then standardized by subtracting the mean from each gene score then dividing by the standard deviation (Z-score).

Gene set enrichment analysis: Gene set enrichment analysis was performed on the set of standardized differential gene scores using the clusterProfiler (v4.2.2) package in R. The gseGO() function was called on the data using all ontologies, min and max GSSsizes set to 10 and 500, respectively, FDR as the p-adjustment method, and an FDR cutoff of 0.01.

Imaging based drug repurposing screen: 384-well, black, optically clear flat-bottom, tissue-culture treated plates (Perkin Elmer cat# 6057302) were coated with 0.1mg/ml of poly-D-lysine hydrobromide (Sigma-Aldrich cat# P6407-5MG) at 37°C for 1hr. Then each plate is washed with molecular grade sterile water once, and then dried at room temperature for 1 hr. Each plate was then dry-spotted with 50nL of 2mM drug solution in DMSO using a Beckman Echo 650 acoustic liquid handler. In each plate, we have 2 columns of vehicle control (Dimethylsulfoxide/DMSO) and 2 columns of Thapsigargin (50 nM) as positive control for inducing endoplasmic reticulum-mitochondrial contact sites. With the plates coated and dry-spotted with drugs, 5000 SW480 colorectal cancer cells were plated in each well with complete DMEM media with a final drug concentration at 2µM. After incubation with the drug for 24 hr, cells were washed with PBS 3 times then fixed with 4% paraformaldehyde (PFA) in 1x PBS (Thermofisher, cat#043368.9M) at room temperature for 15 min in the dark. PFA was removed with 3 PBS washes and the fixed cells were staining with Hoechst 33342 (Invitrogen, cat# H3570, final concentration: 5 µg/ml) and HCS CellMask Deep Red Stain (Invitrogen, cat# H32721, final concentration: 1 µg/ml) for 1 hr at 37°C for 1hr. After staining, the cells were washed with PBS 3 times, and were left in PBS in the dark at 4°C until imaging. Plates were imaged on a Yokogawa CellVoyager 8000 using a 40X/1.0NA water immersion objective lens and nine fields per well were imaged across three channels to visualize Hoechst, GFP, Mitotag RFP and HCS CellMask Deep Red. Cellpose was used to identify nuclei and a custom CellProfiler pipeline was used to delineate the whole cell, mitochondria, GFP spots and per-cell feature extraction was performed. Endoplasmic reticulum–mitochondria contact sites (ERMCS) were identified by counting GFP spots within the cell. A XGBoost machine learning model was trained on centered/scaled cell-level features trained against the negative control (DMSO) and thapsigargin treated positive control wells to enable hit picking. Hits were cherry picked and confirmed with triplicate 10-point/2-fold dilution and EC50 values were fit. Images and details of the screen were deposited to Zenodo and are publicly available in the repository as part of this record: DOI: 10.5281/zenodo.10214159.

Oxygen Consumption Rate (Seahorse): Cells were seeded at 2□×□104 cells/well in 80□µl/well of normal growth media (DMEM with 25□mM Glucose and 2□mM Glutamine) in an Agilent XF96 V3 PS Cell Culture Microplate (#101085-004). To achieve an even distribution of cells within wells, plates were incubated on the bench top at room temperature for 1□h before incubating at 37□°C, 5% CO2 overnight. To hydrate the XF96 FluxPak (#102416-100), 200□µL/well of sterile water was added and the entire cartridge was incubated at 37□°C, no CO2 overnight. The following day, 1□h prior to running the assay, 60□µL/well of growth media was removed from the cell culture plate, and cells were washed twice with 200□µL/well of assay medium (XF DMEM Base Medium, pH 7.4 (#103575-100) containing 25□mM glucose (#103577-100) and 2□mM glutamine (#103579-100)). After washing, 160□µL/well of assay

medium was added to the cell culture plate for a final volume of 180 µL/well. Cells were then incubated at 37 °C, without CO2 until analysis. One hour prior to the assay, water from the FluxPak hydration was exchanged for 200 µL/well of XF Calibrant (#100840-000) and the cartridge was returned at 37 °C, without CO2 until analysis. Oligomycin (100 µM), FCCP (100 µM), and Rotenone/Antimycin (50 µM) from the XF Cell Mito Stress Test Kit (#103015-100) were re-constituted in assay medium to make the indicated stock concentrations. Twenty microliters of Oligomycin was loaded into Port A for each well of the FluxPak, 22 µL of FCCP into Port B, and 25 µL of Rotenone/Antimycin into Port C. Port D was left empty. The final FCCP concentration was optimized to achieve maximal respiration in each condition. The Mito Stress Test was conducted on an XF96 Extracellular Flux Analyzer and OCR was analyzed using Wave 2.6 software. Following the assay, OCR was normalized to cell number utilizing Agilent Cytation5 live cell imaging with Gen5 software.

MT-DNA Quantification: Cells were pelleted, washed 1X in PBS, and then lysed in buffer (25 mM NaOH, 0.2 mM EDTA) for 15 minutes at 95°C. Lysis was neutralized with buffer (40 mM Tris-HCl) and centrifuged at 16,000 x g for 10 minutes at 4°C. Supernatant containing MT-DNA was quantified on with nanodrop. Primers amplifying the MT-DNA marker D-Loop and the nuclear DNA marker β-Globin were used and the relative MT-DNA to nuclear DNA was quantified in each sample[47].

Mitochondria isolation: SW480 and HT1080 cells were scraped and pelleted at 1000 x g for 5 minutes. Cell pellets were washed in 1X PBS and pelleted at 1000 x g for 5 minutes. Cells were re-suspended in isolation buffer (200 mM sucrose, 10 mM Tris HCl, 1 mM EGTA/Tris, pH 7.4 (adjusted with 1M HEPES)), transferred into a 27-gauge needle and homogenized by 10 repeated resuspensions. Homogenates were transferred into tubes and spun at 600 x g for 10 minutes at 4°C. Supernatants were moved to a new tube and centrifugation was repeated. Then, supernatants were moved to a new tube and pelleted at 7,000 x g for 10 minutes at 4°C. Pellets were washed in isolation buffer and centrifugation was repeated two more times. For biochemical analyses, mitochondria were aliquoted in 50 µg pellets.

Flow cytometry for cells: HT1080 and SW480 cells were seeded 48 hr to 72 hr prior to the experiment at 50K and 75K cells density to achieve final 70% confluency by the time of analysis. For analyzing SPLICS and mitoTagRFP intensity, cells were washed, trypsinized, and filtered through a cell strainer prior to analyzing. For MitoSOX Deep Red(Dojindo, cat#: MT14-12), MitoTracker Green (Invitrogen, cat#: M7514), Tetramethylrhodamine, Ethyl Ester, Perchlorate/TMRE (Invitrogen, cat#: T669), and Rhod-2, AM (Invitrogen, cat#: R1244) experiments, cells were stained with 1 µM of MitoSOX Deep Red, 100 nM of MitoTracker Green, 500 nM of TMRE, and 5µM of Rhod-2 for 30 min 37 °C, washed twice with warm PBS, and proceeded with the same processing procedure as unstained cells. Fluorescence activated cell sorting (FACS) was performed on Bigfoot Spectral Cell Sorter (Invitrogen), in which the fluorescence intensity of minimum 10K individual cells was quantified in their specific channel. Data were analyzed using FlowJo software (TreeStar).

Flow cytometry for mitochondria: HT1080 and SW480 cells were seeded at 1.5 million and 3 million in a 15cm plate to achieve final 70% confluency by the time of analysis. Upon 24 hr of treatment with Fedratinib cells were stained with MitoTracker Deep Red or MitoSOX Deep Red. Upon staining, 10% of whole cell fraction was set aside and then mitochondria were isolated with the protocol mentioned. Briefly, cells were fixed at room temperature for 2 min with 2% PFA, and then washed in mitochondria isolation buffer. FACS was performed on Bigfoot Spectral Cell Sorter (Invitrogen), in which the fluorescence intensity of minimum 10K individual cells or 100K

mitochondria was quantified in their specific channel. Data were analyzed using FlowJo software (TreeStar).

Live cell confocal imaging: 35mm glass bottom plates (Ibidi) were coated with 0.1mg/ml of poly-D-Lysine (Sigma) for 1 hour at 37°C, washed once with sterile water, dry in the biosafety cabinet for 2 hours, and then complete media was added on to equilibrate for 20 min in the incubator. 50K of HT1080 and 100K of SW480 cells were then plated to achieve final 60-70% confluency by the time of imaging. Cells with HaloTag-Sec61 were stained with 200nM of JaneliaFluor 646 (JF646, Promega) for 30min at 37°C, and then washed once with warm PBS. Cells were counterstained with 2000x dilution of Hoechst 33342 (Thermofisher) for 15min at 37°C. FluoroBrite DMEM was used as the media for live cell imaging. The cells were imaged using Zeiss LSM 980 Airyscan 2. Post-processing was done with Zen 3.4 (Blue edition).

Proximity ligation assay: Cover glasses (#1.5H Thickness Ø12, Thor Labs) were coated with 0.1mg/ml of poly-D-Lysine (Sigma) for 1 hour at 37°C, washed once with sterile water, dry in the biosafety cabinet for 2 hours, and then complete media was added on to equilibrate for 20 min in the incubator. 25K of HT1080 and 50K of SW480 cells were then plated to achieve final 60-70% confluency by the time of imaging. PLA procedure was conducted via suggested manufacture using Duolink® In Situ Detection Reagents FarRed (Sigma-Aldrich, cat#DUO92013) with primary antibody pairs VDAC1/Porin + VDAC3 and IP3R-I/II/III.

Lattice Light sheet imaging: Same cell conditions were used as live cell confocal imaging. Zeiss Lattice Light Sheet 7 were used and imaged with 20x objective. Cells were treated with Fedratinib and then monitored for 16 hr with images getting acquired every 5 min. Initial post-processing was done with Zen 3.4 (Blue edition). Images were deconvolved and then deskewed in the Zen 3.4. (Deskewing transforms the volume into traditional X, Y, Z coordinates). Then, Arivis Vision 4D (ver. 4.1.0) was used for puncta and cell segmentation. Deconvolved and deskewed datasets were analyzed with Arivis Vision 4D (ver. 4.1.0). For punctas, segmentation was done via the Blob Finder tool. The resulting segments were then filtered by size to remove false positives. For cells, maximum intensity projections of the deconvolved deskewed data were created. Hand segmentations were used to train a machine learning segmentation model. The model was then used to segment each time point in the maximum intensity projection time series. To get the number of cells per time point, the total area of the segments was divided by the average area of a cell. Puncta per cell was then further calculated.

Transmission electron microscopy: SW480 and HT1080 cells treated with vehicle or Fedratinib for 24 hr were fixed in 3% glutaraldehyde and 3% paraformaldehyde in 0.1 M Cacodylate buffer (CB; pH 7.2) overnight at 4 °C. Cells were then washed with PBS and centrifuged at 2000 rpm for 2 mins. Pre-warmed 2% agarose solution was then carefully added to islet pellets, centrifuged and allowed to cool at 4 °C for 30 min. Samples were then subjected to osmification in 1.5% K4Fe(CN)6 + 2% OsO4 in 0.1 CB for 1 h, dehydrated by serial washes in EtOH (30%, 50%, 70%, 80%, 90%, 95% and 100%) and embedded in Spurr's resin by polymerization at 60 °C for 24 h. Polymerized resins were then sectioned at 90 nm thickness using a Leica EM UC7 ultramicrotome and imaged at 70 kV using a JEOL 1400 TEM equipped with an AMT CMOS imaging system. Cristae classifications were done by blinding all images, and then manually annotated with the four cristae classification: laminar, non-laminar, compartmentalized, and loss-of-cristae. Mitochondrial structures (Aspect Ratio, Perimeter, Circularity) were analyzed and quantified by Fiji/ImageJ. A minimum of 150 mitochondria are analyzed from 25 independent cells.

Correlative light and electron microscopy (CLEM): SW480 SPLICS reporter cells were induced with doxycycline (100 ng/ml) for 24 hr, and then treated with Fedratinib for 24 hr. EM preparation and image acquisition were performed based on this paper [48]

Segmentation for CLEM: Automated detection of membranes in the tomogram was performed using the TomoSegMemTV (April 2020 version) software package (PMID: 24625523). The parameters used for membrane enhancement were as follows: scale_space -s 3; dtvoting -s 10 (default); surfaceness -m 0.45 -s 1.0 -p 1.0 (default); dtvoting -w -s 10 (default); surfaceness -S -m 0.3 (default); thresholding -l 0.05; global analysis −3 100 (default). The output volumes were imported into AMIRA 2022.2 (Thermo Fisher Scientific), and segmented membrane pixels were manually annotated as specific organelle membranes using the 3D magic wand tool and saved as different labels. Further, gaps in the segmentation were filled using the paint tool. The final membrane surfaces were generated using the 'generate surface' module and smoothened using the 'smooth surface' module with the following parameters: iterations 100; lambda 0.2.

Sample preparation for LC-MS/MS metabolomics and lipidomics analysis: Samples for metabolomics and lipidomics LC-MS/MS analyses were prepared by following the automated dual-metabolite/lipid sample preparation workflow described in the Agilent application note 5994-5065EN. Briefly, cells (ca. 1M) were collected, washed with PBS and lysed with 1:1 trifluoroethanol/water at room temperature. Lysates were transferred to microcentrifuge tubes, incubated for 10 minutes, quickly centrifuged at 250 xg for 30 seconds, and dried out by centrifugation under reduced pressure with no heat. Samples were resuspended with 1:1 trifluoroethanol/water, transferred to a 96-well plate, and processed on a Bravo Metabolomics sample preparation platform (Agilent Technologies, Inc.) with two separate VWorks protocols to sequentially and selectively isolate cell metabolites and lipids as described (5994-5065EN).

LC-MS/MS metabolomics and lipidomics analysis: Sample were analyzed on an Agilent 1290 Infinity II Bio LC ultra-high performance liquid chromatography (UPLC) system consisting of a high-pressure binary pump, multicolumn thermostat, and a temperature controlled multisampler. The LC modules were setup with a standard configuration for omics workflows, which allowed easy acquisition method interchange for polar metabolites and lipid analyses. Samples for both targeted metabolomics and lipidomics analysis were analyzed in randomized order on an Agilent 6495C triple quadrupole mass spectrometer equipped with an Agilent Jet Stream Dual ESI ion source. For targeted metabolomics, isolated polar metabolites were analyzed with a HILIC LC-MS/MS method as described in the Agilent application note 5994-5628EN. For targeted lipidomics analysis, samples were analyzed with the reverse phase LC-MS/MS method reported in the Agilent application note 5994-3747EN. After acquisition, both metabolomics and lipidomics datasets were processed with MassHunter Quantitative analysis software and subsequently imported into Mass Profiler Professional (MPP) for chemometrics analysis. Metabolomics and lipidomics data were analyzed using MetaboAnalyst. In particular, statistical analysis [one factor] was selected. Data table with metabolite peak intensities in rows and samples in column was used. Data were filtered based on interquartile range (IQR) set filter out 25%, normalized based on protein quantitation, transformed with Log base 10, scaled by mean-centering and dividing by the standard deviation of each variable. Data were visualized with principal component anlysis (PCA) and volcano plots.

Mitochondrial lipidomics: Mitochondria were isolated with the same method detailed prior. The samples were thawed on ice and mixed with 1 mL of IPA:Water:EtOAc containing 2 mM EquiSPLASH LIPIDOMIX Quantitative Mass Spec Internal Standard (Avanti Polar Lipids, Birmingham, AL). This mixture was vortexed, sonicated for 2 min, and centrifuged for 10 min at 8000 × g at 4 °C. The organic upper phase was transferred to a new tube. The pellet was re-

extracted with additional 0.5 mL of IPA:Water:EtOAc. The supernatants from the extracts were combined and placed at -20 °C for a day. The combined supernatants were dried down in a vacuum (SpeedVac) and then reconstituted in Solvent A of LC conditions, with a reconstitution volume of 150 µL. The reconstituted sample was vortexed, sonicated for complete resuspension, and centrifuged for 10 min at 17,000 × g at 4 °C. Finally, the supernatant was transferred to an auto-sampler vial for UHPLC-MS analysis.

Samples were analyzed by Vanquish UHPLC system coupled with an Orbitrap Fusion Lumos Tribrid™ mass spectrometer using a H-ESI™ ion source (all Thermo Fisher Scientific) with a Waters (Milford, MA) CSH C18 column (1.0 × 150 mm, 1.7 µm particle size). Solvent A is ACN:H2O (60:40; v/v) containing 10 mM Ammonium formate and 0.1 % formic acid and solvent B is IPA:ACN (95:5; v/v) containing 10 mM Ammonium formate and 0.1 % formic acid. Flow rate of mobile phase is 0.11 mL/min with column temperature of 65 °C. The gradient of solvent B is 0 min 15% (B), 0–2 min 30% (B), 2–2.5 min 48% (B), 2.5–11 min 82% (B), 11–11.01 min 99% (B), 11.01–12.95 min 99% (B), 12.95–13 min 15% (B), and 13–15 min 15% (B). Ion source spray voltages are 4,000 V in positive mode. The mass spectrometry was conducted with scan range from 200 to 1500 m/z for full scan and MS1 resolution was set to 120K at m/z 200. MS/MS spectrum was acquired with AcquireX mode and stepped collision energy of 30 % with 15 % spread for fragment ion MS/MS scan.

<u>Targeted CoQ Measurement by LC-MS/MS:</u> Determination of the CoQ content and redox state in mammalian cell culture and isolated mitochondria (with described isolation process) was performed as previously described with modifications. In brief, frozen cell pellets or mitochondria pellets were resuspended in 200 µL of PBS and added to ice cold extraction solution (200 µL acidified methanol [0.1% HCl final], 300 µL hexane, with 0.1 µM CoQ_8 internal standard). Samples were vortexed and centrifuged (5 min, 17000 x g, 4°C) and the top hexane layer was transferred to a new tube. Extraction was repeated twice before the hexane layers were combined and dried under argon gas at room temperature. Extracted dried lipids were resuspended in methanol containing 2 mM ammonium formate and overlaid with argon.

LC-MS analysis was performed using a Thermo Vanquish Horizon UHPLC system coupled to a Thermo Exploris 240 Orbitrap mass spectrometer. For LC separation, a Vanquish binary pump system (Thermo Fisher Scientific) was used with a Waters Acquity CSH C18 column (100 mm × 2.1 mm, 1.7 µm particle size) held at 35 °C under 300 µL/min flow rate. Mobile phase A consisted of 5 mM ammonium acetate in acetonitrile:H_2O (70:30, v/v) with 125 µL/L acetic acid. Mobile phase B consisted of 5 mM ammonium acetate in isopropanol:acetonitrile (90:10, v/v) with the same additive. For each sample run, mobile phase B was initially held at 2% for 2 min and then increased to 30% over 3 min. Mobile phase B was further increased to 50% over 1 min and 85% over 14 min and then raised to 99% over 1 min and held for 4 min. The column was re-equilibrated for 5 min at 2% B before the next injection. Five microliters of the sample were injected by a Vanquish Split Sampler HT autosampler (Thermo Fisher Scientific), while the autosampler temperature was kept at 4 °C. The samples were ionized by a heated ESI source kept at a vaporizer temperature of 350 °C. Sheath gas was set to 50 units, auxiliary gas to 8 units, sweep gas to 1 unit, and the spray voltage was set to 3500 V for positive mode and 2500 V for negative mode. The inlet ion transfer tube temperature was kept at 325 °C with 70% RF lens. For targeted analysis, the MS was operated in parallel reaction monitoring mode with polarity switching acquiring scheduled, targeted scans to oxidized CoQ_{10} H+ adduct (m/z 863.6912), oxidized CoQ_{10} NH+ adduct (m/z 880.7177), reduced $CoQ_{10}H_2$ H+ adduct (m/z 865.7068), reduced $CoQ_{10}H_2$ NH+ adduct (m/z 882.7334), CoQ_8 H+ adduct (m/z 727.566) and CoQ intermediates: DMQ_{10} H+ adduct (m/z 833.6806), and $PPHB_{10}$ H- adduct (m/z 817.6504). MS acquisition parameters include resolution of 15,000, HCD collision energy (30% for positive

mode and stepped 20%, 40%, 60% for negative mode), and 3s dynamic exclusion. Automatic gain control targets were set to standard mode. The resulting CoQ intermediate data were processed using TraceFinder 5.1 (Thermo Fisher Scientific). Raw intensity values were normalized to the CoQ_8 internal standard and protein content as determined by BCA[49].

RNA Extraction, Reverse Transcription, Real-time PCR and Bromouridine nascent mRNA-Sequencing: RNA was extracted from SW480 and HT1080 cells using the QIAGEN RNeasy mini kit according to the manufacturer's instructions. 1 ug of RNA was reverse transcribed using the Lunascript Supermix (NEB) according to the manufacturer's instructions. Quantitative real-time PCR (qPCR) was performed using SYBR green master mix and beta actin (ACTB) was used as a control. The primer sequences are listed in Supplementary Table 5. BrU-Seq method is described in this paper[50].

Reproducibility: Each cell line experiment was performed in technical replicates for each condition and repeated at least three times with biological triplicates to ensure reproducibility. Figures show a representative biological replicate unless otherwise indicated. Blinding was performed whenever appropriate. Sample description and identification was unavailable to the core personnel during data collection and analysis. Statistical details of all experiments can be found in the figure legends. The sample numbers are mentioned in each figure legend and denote biological replicates. Statistical details are reported in figure legends. Results are expressed as the mean plus or minus the standard error of the mean for all figures unless otherwise noted. Significance between 2 groups was tested using a 2 tailed unpaired t test. Significance among multiple groups was tested using a one-way ANOVA. GraphPad Prism 7.0 was used for the statistical analysis. Statistical significance is described in the figure legends as: $*$ $p < 0.05$, $**$ $p < 0.01$, $***$ $p < 0.001$, $****$ $p < 0.0001$.

Data availability: Images and details of the image-based drug repurposing screen were deposited to Zenodo and are publicly available in the repository as part of this record: DOI: 10.5281/zenodo.10214159. Datasets generated are also available from the corresponding author upon reasonable request.

Figure Illustrations: Figure were created using Adboe Illustrator and Biorender.com.

Drug treatment: Small molecule inhibitors used in this studied are listed in the following table. Concentration of each compound is listed in figure legend other than Fedratinib. Fedratinib was used at 1 μM for all studies unless indicated differently.

Compound	**Company**	**Catalog number**
Fedratinib	MedChem Express	HY-10309
Thapsigargin	Cayman Chemicals	10522
Ruxolitinib	Cayman Chemicals	11609
dBET6	Cayman Chemicals	35385
Actinomycin D	Cayman Chemicals	11421
AS-2863619	Cayman Chemicals	30976
NVP2	Cayman Chemicals	34725
Piericidin A	Cayman Chemicals	15379
TTFA	Cayman Chemicals	15517
Antimycin A	Cayman Chemicals	34799
Myxothiazol	Sigma Aldrich	T5580
Oligomycin	Cayman Chemicals	11341

CCCP	Cayman Chemicals	25458
FG4592	Cayman Chemicals	15294
MitoPQ	Cayman Chemicals	18808

References:

1. Eisenberg-Bord, M., Shai, N., Schuldiner, M. & Bohnert, M. A Tether Is a Tether Is a Tether: Tethering at Membrane Contact Sites. *Dev. Cell* **39**, 395–409 (2016).

2. Scorrano, L. *et al.* Coming together to define membrane contact sites. *Nat Commun* **10**, 1287 (2019).

3. Shiao, Y. J., Balcerzak, B. & Vance, J. E. A mitochondrial membrane protein is required for translocation of phosphatidylserine from mitochondria-associated membranes to mitochondria. *Biochem. J.* **331 (Pt 1)**, 217–23 (1998).

4. Hajnóczky, G., Robb-Gaspers, L. D., Seitz, M. B. & Thomas, A. P. Decoding of cytosolic calcium oscillations in the mitochondria. *Cell* **82**, 415–424 (1995).

5. Friedman, J. R. *et al.* ER Tubules Mark Sites of Mitochondrial Division. *Science* **334**, 358–362 (2011).

6. Prudent, J. *et al.* MAPL SUMOylation of Drp1 Stabilizes an ER/Mitochondrial Platform Required for Cell Death. *Mol. Cell* **59**, 941–955 (2015).

7. Lewis, S. C., Uchiyama, L. F. & Nunnari, J. ER-mitochondria contacts couple mtDNA synthesis with mitochondrial division in human cells. *Science* **353**, aaf5549 (2016).

8. Hamasaki, M. *et al.* Autophagosomes form at ER–mitochondria contact sites. *Nature* **495**, 389–393 (2013).

9. Lee, K.-S. *et al.* Altered ER–mitochondria contact impacts mitochondria calcium homeostasis and contributes to neurodegeneration in vivo in disease models. *Proc. Natl. Acad. Sci.* **115**, E8844–E8853 (2018).

10. Arruda, A. P. *et al.* Chronic enrichment of hepatic endoplasmic reticulum–mitochondria contact leads to mitochondrial dysfunction in obesity. *Nat Med* **20**, 1427–1435 (2014).

11. Çoku, J. *et al.* Reduced ER–mitochondria connectivity promotes neuroblastoma multidrug resistance. *EMBO J.* **41**, e108272 (2022).

12. Thoudam, T. *et al.* PDK4 Augments ER–Mitochondria Contact to Dampen Skeletal Muscle Insulin Signaling During Obesity. *Diabetes* **68**, 571–586 (2019).

13. Rodríguez, L. R. *et al.* Oxidative stress modulates rearrangement of endoplasmic reticulum-mitochondria contacts and calcium dysregulation in a Friedreich's ataxia model. *Redox Biol.* **37**, 101762 (2020).

14. Vallese, F. *et al.* An expanded palette of improved SPLICS reporters detects multiple organelle contacts in vitro and in vivo. *Nat Commun* **11**, 6069 (2020).

15. Cieri, D. *et al.* SPLICS: a split green fluorescent protein-based contact site sensor for narrow and wide heterotypic organelle juxtaposition. *Cell Death Differ* **25**, 1131–1145 (2017).

16. Calì, T. *et al.* splitGFP Technology Reveals Dose-Dependent ER-Mitochondria Interface Modulation by α-Synuclein A53T and A30P Mutants. *Cells* **8**, 1072 (2019).

17. Giamogante, F. *et al.* Stable Integration of Inducible SPLICS Reporters Enables Spatio-Temporal Analysis of Multiple Organelle Contact Sites upon Modulation of Cholesterol Traffic. *Cells* **11**, 1643 (2022).

18. Mishra, P., Carelli, V., Manfredi, G. & Chan, D. C. Proteolytic Cleavage of Opa1 Stimulates Mitochondrial Inner Membrane Fusion and Couples Fusion to Oxidative Phosphorylation. *Cell Metab* **19**, 630–641 (2014).

19. Bravo, R. *et al.* Increased ER–mitochondrial coupling promotes mitochondrial respiration and bioenergetics during early phases of ER stress. *J Cell Sci* **124**, 2143–2152 (2011).

20. Hertlein, V. *et al.* MERLIN: a novel BRET-based proximity biosensor for studying mitochondria–ER contact sites. *Life Sci Alliance* **3**, e201900600 (2019).

21. Cole, N. B. & Lippincott-Schwartz, J. Organization of organelles and membrane traffic by microtubules. *Curr. Opin. Cell Biol.* **7**, 55–64 (1995).

22. Talpaz, M. & Kiladjian, J.-J. Fedratinib, a newly approved treatment for patients with myeloproliferative neoplasm-associated myelofibrosis. *Leukemia* **35**, 1–17 (2021).

23. Wernig, G. *et al.* Efficacy of TG101348, a Selective JAK2 Inhibitor, in Treatment of a Murine Model of JAK2V617F-Induced Polycythemia Vera. *Cancer Cell* **13**, 311–320 (2008).

24. Hantschel, O. Unexpected Off-Targets and Paradoxical Pathway Activation by Kinase Inhibitors. *ACS Chem. Biol.* **10**, 234–245 (2015).

25. Ciceri, P. *et al.* Dual kinase-bromodomain inhibitors for rationally designed polypharmacology. *Nat Chem Biol* **10**, 305–312 (2014).

26. Kleppe, M. *et al.* Dual Targeting of Oncogenic Activation and Inflammatory Signaling Increases Therapeutic Efficacy in Myeloproliferative Neoplasms. *Cancer Cell* **33**, 29-43.e7 (2018).

27. Hinton, A. *et al.* A Comprehensive Approach to Sample Preparation for Electron Microscopy and the Assessment of Mitochondrial Morphology in Tissue and Cultured Cells. *Adv. Biol.* **7**, e2200202 (2023).

28. Venkatraman, K. *et al.* Cristae formation is a mechanical buckling event controlled by the inner mitochondrial membrane lipidome. *EMBO J.* e114054 (2023) doi:10.15252/embj.2023114054.

29. Baik, A. H. & Jain, I. H. Turning the Oxygen Dial: Balancing the Highs and Lows. *Trends Cell Biol.* **30**, 516–536 (2020).

30. Spinelli, J. B. *et al.* Fumarate is a terminal electron acceptor in the mammalian electron transport chain. *Science* **374**, 1227–1237 (2021).

31. Geng, J. *et al.* Deregulation of ER-mitochondria contact formation and mitochondrial calcium homeostasis mediated by VDAC in fragile X syndrome. *Dev. Cell* **58**, 597-615.e10 (2023).

32. Filippakopoulos, P. *et al.* Selective inhibition of BET bromodomains. *Nature* **468**, 1067–1073 (2010).

33. Barrow, J. J. *et al.* Bromodomain Inhibitors Correct Bioenergetic Deficiency Caused by Mitochondrial Disease Complex I Mutations. *Mol. Cell* **64**, 163–175 (2016).

34. Sakamaki, J. *et al.* Bromodomain Protein BRD4 Is a Transcriptional Repressor of Autophagy and Lysosomal Function. *Mol. Cell* **66**, 517-532.e9 (2017).

35. Costa-Mattioli, M. & Walter, P. The integrated stress response: From mechanism to disease. *Science* **368**, (2020).

36. Kalkavan, H. *et al.* Sublethal cytochrome c release generates drug-tolerant persister cells. *Cell* **185**, 3356-3374.e22 (2022).

37. Palchaudhuri, R. *et al.* A Small Molecule that Induces Intrinsic Pathway Apoptosis with Unparalleled Speed. *Cell Rep.* **13**, 2027–2036 (2015).

38. Chipuk, J. E. *et al.* Sphingolipid Metabolism Cooperates with BAK and BAX to Promote the Mitochondrial Pathway of Apoptosis. *Cell* **148**, 988–1000 (2012).

39. Verfaillie, T. *et al.* PERK is required at the ER-mitochondrial contact sites to convey apoptosis after ROS-based ER stress. *Cell Death Differ* **19**, 1880–1891 (2012).

40. Stefely, J. A. & Pagliarini, D. J. Biochemistry of Mitochondrial Coenzyme Q Biosynthesis. *Trends Biochem. Sci.* **42**, 824–843 (2017).

41. Bersuker, K. *et al.* The CoQ oxidoreductase FSP1 acts parallel to GPX4 to inhibit ferroptosis. *Nature* **575**, 688–692 (2019).

42. Doll, S. *et al.* FSP1 is a glutathione-independent ferroptosis suppressor. *Nature* **575**, 693–698 (2019).

43. Jones, M. E. Pyrimidine Nucleotide Biosynthesis in Animals: Genes, Enzymes, and Regulation of UMP Biosynthesis. *Annu. Rev. Biochem.* **49**, 253–279 (1980).

44. Kumar, R. *et al.* A redox cycle with complex II prioritizes sulfide quinone oxidoreductase-dependent H2S oxidation. *J. Biol. Chem.* **298**, 101435 (2022).

45. Guerra, R. M. & Pagliarini, D. J. Coenzyme Q biochemistry and biosynthesis. *Trends Biochem Sci* **48**, 463–476 (2023).

46. Williams, R. T. *et al.* ZBTB1 Regulates Asparagine Synthesis and Leukemia Cell Response to L-Asparaginase. *Cell Metab.* **31**, 852-861.e6 (2020).

47. Chan, S. W. & Chen, J. Z. Measuring mtDNA damage using a supercoiling-sensitive qPCR approach. *Methods Mol. Biol. (Clifton, NJ)* **554**, 183–97 (2009).

48. Ronchi, P. *et al.* High-precision targeting workflow for volume electron microscopy. *J. Cell Biol.* **220**, e202104069 (2021).

49. Burger, N. *et al.* A sensitive mass spectrometric assay for mitochondrial CoQ pool redox state in vivo. *Free Radic. Biol. Med.* **147**, 37–47 (2020).

50. Paulsen, M. T. *et al.* Use of Bru-Seq and BruChase-Seq for genome-wide assessment of the synthesis and stability of RNA. *Methods* **67**, 45–54 (2014).

Acknowledgments: We thank all members of the Shah and Lyssiotis labs for their advice and suggestions. In collaboration with this research, we acknowledge support from the University of Michigan Biomedical Research Core Facilities (Flow Cytometry core, Advanced Genomics core, Microscopy core), and Bru-seq Lab. The funders (Agilent Technologies) for the whole cell metabolomics and lipidomics had no role in study design, data collection and analysis, or the content and publication of this manuscript. We acknowledge the European Molecular Biology Laboratory (EMBL) Electron Microscopy Core Facilities' assistance, data acquisition, and analysis for CLEM expertise. B.C was supported by NCI F99CA284256-01. Y.M.S. was supported by NCI R01CA148828, R01CA245546, and NIDDK R01DK095201. C.A.L. was supported by NCI R37CA237421, R01CA248160, and R01CA244931. S.M. was supported by NIGMS DP2GM150019. D.J.P. was supported by NIDDK R01DK098672 and NIGMS R35GM131795. N.J.R. was supported by NIGMS T32GM145470 and T32GM150581. R.B. was supported by NIGMS R35GM130183. D.A.H. was supported by NIGMS F32GM140694. A.D.P. was supported by NIH S10OD021750, USDA National Institute of Food and Federal Appropriations Project PEN047702, and Pennsylvania Department of Health using Tobacco CURE funds. T.C was supported by Italian Ministry of University and Research PRIN2017, University of Padova STARS Consolidator Grant 2019 and Progetto di Ateneo 2023 no. CALI_BIRD23_01, and PNRR – CN3 National Center for Gene Therapy and Drugs based on RNA Technology n. CN00000041 (2022-26).

Author contributions: B.C., C.A.L., and Y.M.S. designed the study and wrote the manuscript. B.C. designed experiments and collected data for the bulk of the experimental studies. B.C., T.M.L., P.J., B.S.H., N.J.R., R.M.G., I.K., P.M., D.A.H., and J.L. carried out experimental aspects of the project, and contributed to data analysis. B.C., S.M., D.J.P., N.J.R., R.B., D.A.H., T.C., C.A.L., and Y.M.S. provided resources, funding, and conceptual input for experiments and supervised the research. All authors are involved in the throughout the research process, agreed amongst authors regarding roles and responsibilities, and contributed to review, editing, and approval of the manuscript.

Conflicting interests: In the past three years, C.A.L. has consulted for Astellas Pharmaceuticals, Odyssey Therapeutics, Third Rock Ventures, and T-Knife Therapeutics, and is an inventor on patents pertaining to Kras regulated metabolic pathways, redox control pathways in pancreatic cancer, and targeting the GOT1-ME1 pathway as a therapeutic approach (US Patent No: 2015126580-A1, 05/07/2015; US Patent No: 20190136238, 05/09/2019; International Patent No: WO2013177426-A2, 04/23/2015).

Materials & Correspondence: Supplementary Information is available for this paper. All data generated or analyzed during this study are included in this published article and its supplementary information files. Correspondence and requests for materials should be addressed to Yatrik M. Shah (shahy@umich.edu) or Costas A. Lyssiotis (clyssiot@med.umich.edu).

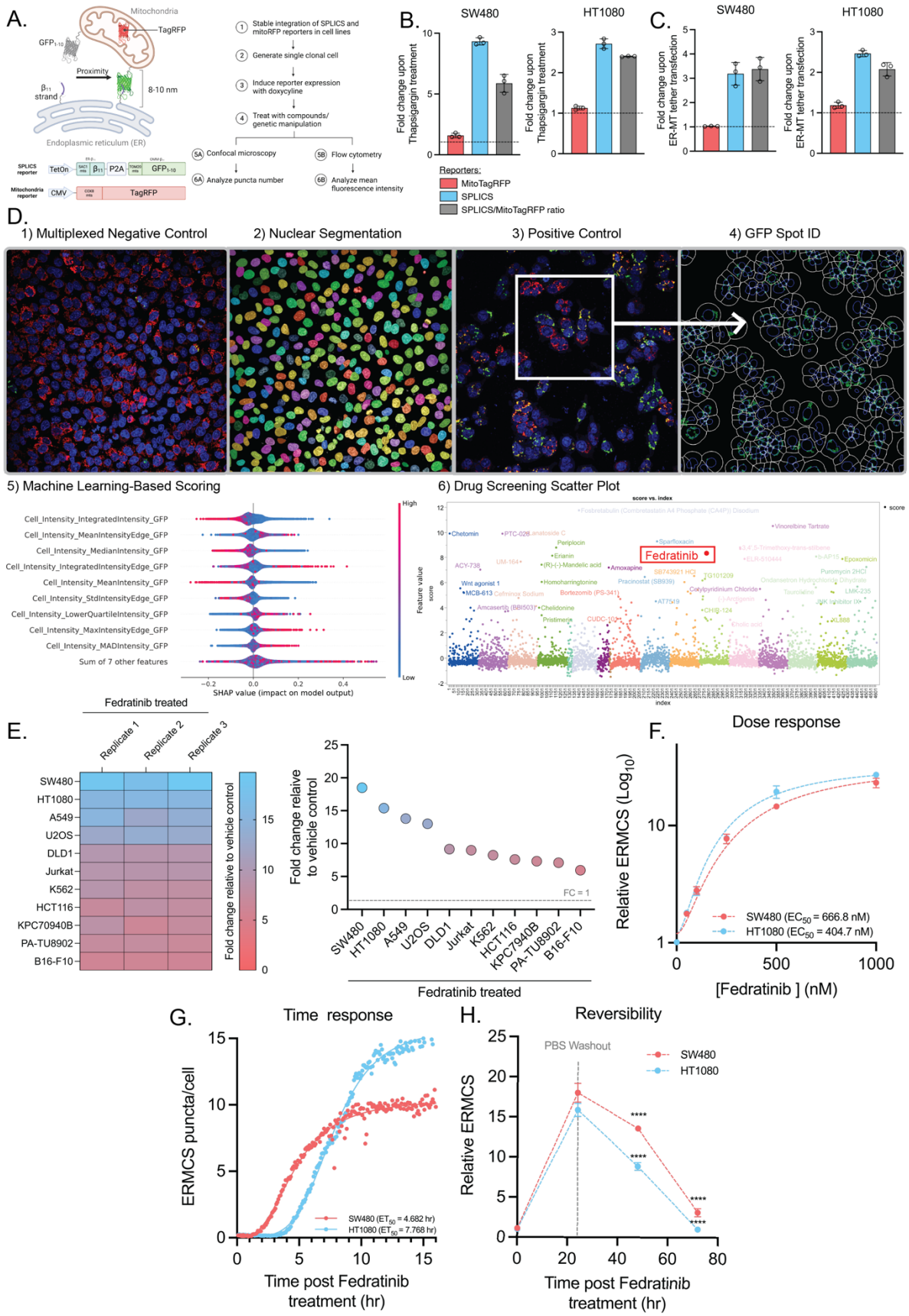
A.
Mitochondria
TagRFP
GFP1-10
Proximity
β11 strand
8-10 nm
Endoplasmic reticulum (ER)
SPLICS reporter
TetOn
β11
P2A
GFP1-10
Mitochondria reporter
CMV
TagRFP
1 Stable integration of SPLICS and mitoRFP reporters in cell lines
2 Generate single clonal cell
3 Induce reporter expression with doxycyline
4 Treat with compounds/ genetic manipulation
5A Confocal microscopy
6A Analyze puncta number
5B Flow cytometry
6B Analyze mean fluorescence intensity
B.
SW480
HT1080
Fold change upon Thapsigargin treatment
C.
SW480
HT1080
Fold change upon ER-MT tether transfection
Reporters:
MitoTagRFP
SPLICS
SPLICS/MitoTagRFP ratio
D.
1) Multiplexed Negative Control
2) Nuclear Segmentation
3) Positive Control
4) GFP Spot ID
5) Machine Learning-Based Scoring
Cell_Intensity_IntegratedIntensity_GFP
Cell_Intensity_MeanIntensityEdge_GFP
Cell_Intensity_MedianIntensity_GFP
Cell_Intensity_IntegratedIntensityEdge_GFP
Cell_Intensity_MeanIntensity_GFP
Cell_Intensity_StdIntensityEdge_GFP
Cell_Intensity_LowerQuartileIntensity_GFP
Cell_Intensity_MaxIntensityEdge_GFP
Cell_Intensity_MADIntensity_GFP
Sum of 7 other features
SHAP value (impact on model output)
High
Low
Feature value
6) Drug Screening Scatter Plot
score vs. index
Fedratinib
score
index
E.
Fedratinib treated
Replicate 1
Replicate 2
Replicate 3
SW480
HT1080
A549
U2OS
DLD1
Jurkat
K562
HCT116
KPC70940B
PA-TU8902
B16-F10
Fold change relative to vehicle control
Fold change relaive to vehicle control
FC = 1
Fedratinib treated
F.
Dose response
Relative ERMCS (Log10)
SW480 (EC50 = 666.8 nM)
HT1080 (EC50 = 404.7 nM)
[Fedratinib] (nM)
G.
Time response
ERMCS puncta/cell
SW480 (ET50 = 4.682 hr)
HT1080 (ET50 = 7.768 hr)
Time post Fedratinib treatment (hr)
H.
Reversibility
PBS Washout
SW480
HT1080
Relative ERMCS
Time post Fedratinib treatment (hr)

868

Fig. 1. High throughput image-based chemical screen identifies novel regulators of ERMCS.

(**A**) Schematic of the SPLICS and mitochondria TagRFP (mitoTagRFP) reporter and analysis pipeline for ERMCS. (**B**) Relative fluorescence intensity of SPLICS, mitoTagRFP, and SPLICS/mitoTagRFP ratio following treatment with vehicle or thapsigargin (50 nM) for 24 hr, or (**C**) 48 hr post transfection of ER-MT tether. (**D**) D. Schematic representation of the bioassay design for the ERMCS drug screen. Clockwise: 1. Negative control demonstrating low levels of ERMCS; 2. Cellpose nuclear segmentation using Hoechst counterstain; 3. Positive control demonstrating induction of high levels of ERMCS. 4. GFP spot identification and feature extraction using Cellprofiler for ERMCS. Machine learning was performed by training an XGBoost model against per-plate controls. 5. Shapley additive explanations showing GFP features used to identify hits in drug screening. Beeswarm plot showing SHAP values indicating feature importance for drug effect scoring based on GFP features. 6. Drug screening scatter plot showing drug tested on the x-axis and XGBoost score on the y-axis indicating ERMCS induction. Fedratinib is highlighted in red on the scatter plot. (**E**) Relative ERMCS in a panel of cell lines treated with vehicle or fedratinib treatment for 24 hr. (**F**) Relative ERMCS of cells treated with vehicle or fedratinib for 24 hr, followed by PBS washout, and monitored for additional 48 hr. (**G**) Dose dependent increase of relative ERMCS of cells treated with vehicle or fedratinib for 24 hr. **(H)** Time-lapse imaging using Lattice light sheet microscopy to monitor ERMCS puncta of cells treated with fedratinib for 16 hr with quantified puncta per cell. For ERMCS measurement with flow cytometry (**B**, **C**, **E**, **F**, **G**), 3 independent experiments were performed. Significance was calculated with an unpaired two-tailed t-test. *$P \leq 0.05$, **$P \leq 0.01$, ***$P \leq 0.001$, ****$P \leq 0.0001$. Data are mean ± SD.

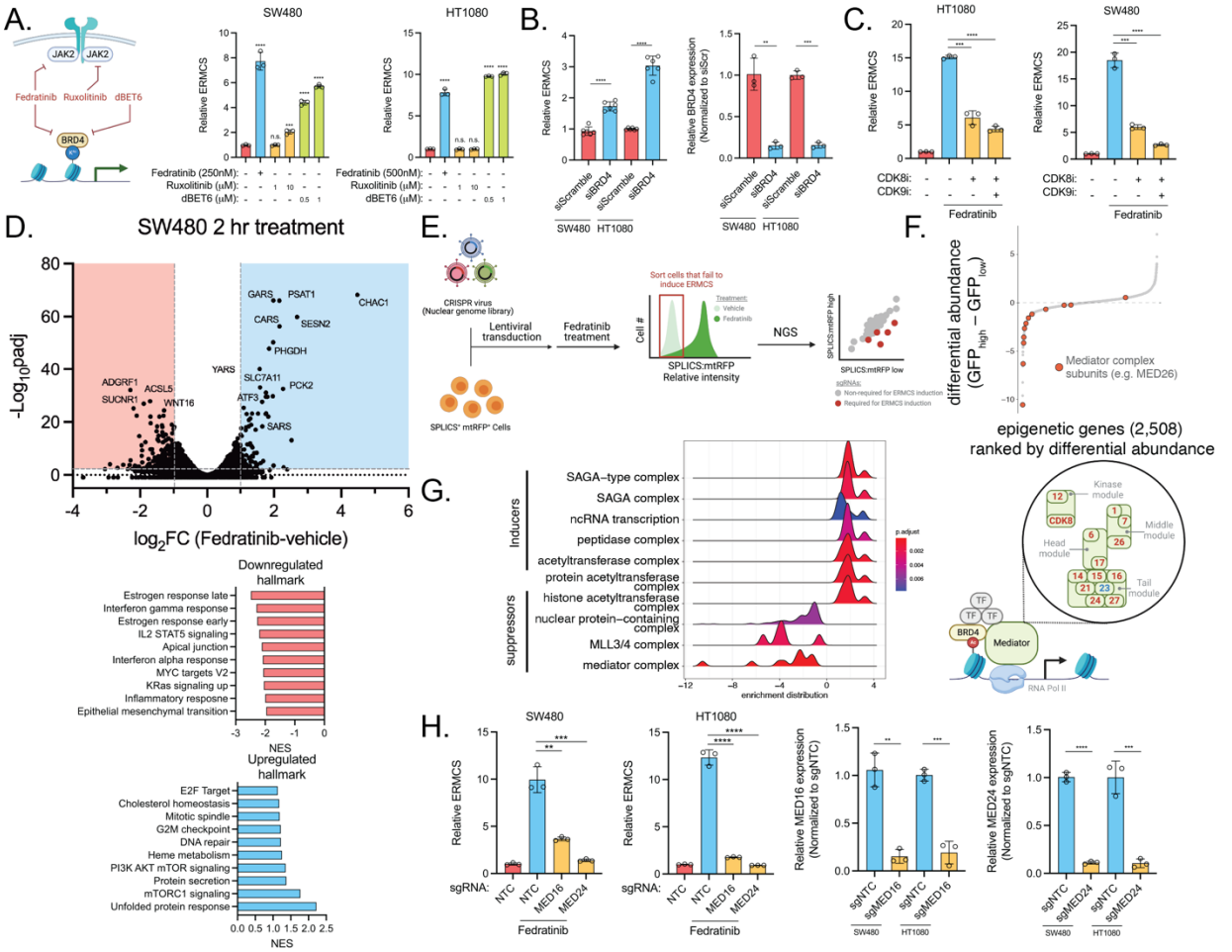

Fig. 2. ERMCS induction requires a transcriptional response dependent on bromodomain and extra-terminal protein (BET).

(**A**) Mechanisms of action for fedratinib, ruxolitinib, and dBET6 targeting JAK2 and BRD4 (Left). Relative ERMCS in cells treated with JAK2 and/or BRD4 inhibitors. (**B**) Relative ERMCS and BRD4 mRNA expression of cells following knockdown (KD) using scrambled or BRD4 targeting siRNAs. (**C**) Relative ERMCS in cells treated with inhibitors of transcription kinase CDK8 (AS-2863619, 1 μM) or CDK9 (NVP2, 1 μM) for 6 hr, and then treated with vehicle or fedratinib for 24 hr. (**D**) Volcano plot of BrU-seq analysis after SW480 cells treated with fedratinib for 2 hr (top panel). Normalized enrichment score (NES) of top pathways altered (bottom panel). (**E**) Schematic of a Fluorescence-activated cell sorting (FACS)-based CRISPR screen using a nuclear genome targeted sgRNA library. (**F**) CRISPR gene scores highlighting sgRNAs targeting the Mediator complex components (Top panel). Schematic of the mediator complex and BRD4 in transcriptional regulation. Mediator components from the CRISPR library, annotated in red demonstrate suppression of ERMCS (Bottom panel). (**G**) GSEA ridgeplot displaying significantly enriched (FDR < 0.01) protein complexes based on differential CRISPR screen scores. (**H**) Relative ERMCS and gene expression level of MED16 and MED24 mRNA transcripts upon CRISPRi mediated knockdown of cells treated with vehicle or fedratinib for 24 hr. For ERMCS measurement with flow cytometry (**A**, **B**, **C**, **H**) and qRT-PCR (**B**, **H**) 3 independent experiments were performed. Significance was calculated with an unpaired two-tailed t-test. n.s. = not significant, *P ≤ 0.05, **P ≤ 0.01, ***P ≤ 0.001, ****P ≤ 0.0001. Data are mean ± SD.

916

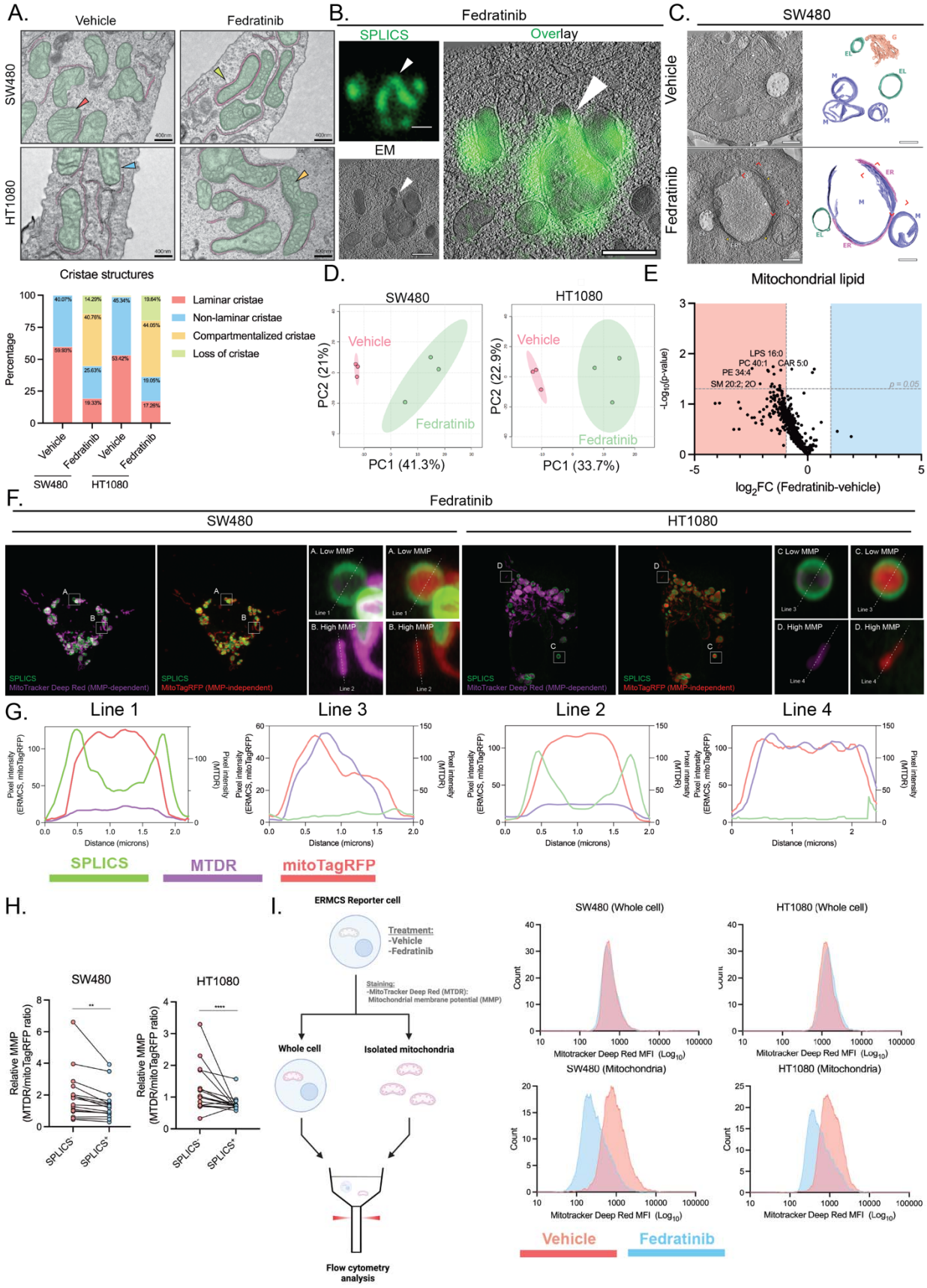
A.
Vehicle
Fedratinib
SW480
HT1080
B.
Fedratinib
SPLICS
Overlay
EM
C.
SW480
Vehicle
Fedratinib
Cristae structures
Percentage
Laminar cristae
Non-laminar cristae
Compartmentalized cristae
Loss of cristae
D.
SW480
HT1080
PC2 (21%)
PC1 (41.3%)
PC2 (22.9%)
PC1 (33.7%)
E
Mitochondrial lipid
LPS 16:0
PC 40:1
CAR 5:0
PE 34:4
SM 20:2; 2O
p = 0.05
-Log10(p-value)
log2FC (Fedratinib-vehicle)
F.
Fedratinib
SW480
HT1080
SPLICS
MitoTracker Deep Red (MMP-dependent)
MitoTagRFP (MMP-independent)
A. Low MMP
B. High MMP
C Low MMP
D. High MMP
G.
Line 1
Line 3
Line 2
Line 4
Pixel intensity (ERMCS, mitoTagRFP)
Pixel intensity (MTDR)
Distance (microns)
SPLICS
MTDR
mitoTagRFP
H.
SW480
HT1080
Relative MMP (MTDR/mitoTagRFP ratio)
SPLICS-
SPLICS+
I.
ERMCS Reporter cell
Treatment:
-Vehicle
-Fedratinib
Staining:
-MitoTracker Deep Red (MTDR):
Mitochondrial membrane potential (MMP)
Whole cell
Isolated mitochondria
Flow cytometry analysis
SW480 (Whole cell)
HT1080 (Whole cell)
SW480 (Mitochondria)
HT1080 (Mitochondria)
Count
Mitotracker Deep Red MFI (Log10)
Vehicle
Fedratinib

917

Fig. 3. Fedratinib induces novel ultrastructural changes at ERMCS and selective depolarization of ER-wrapped mitochondria.
(**A**) Representative TEM images (scale bar: 400 nm) of WT cells treated with vehicle or fedratinib for 24 hr (Mitochondria green, ER: magenta (Above)). Distribution of cristae morphologies quantified from 25 cells as a percentage of total mitochondria (n=161-299). Cristae structures are annotated in corresponding colors in the stacked bars with percentage of each classification listed. Red: Laminar cristae. Blue: Non-laminar cristae. Yellow: Compartmentalized cristae. Green: Loss of cristae (Below). Each example cristae structure is indicated with its corresponding color in the EM images. (**B**) Correlative light and electron microscopy (CLEM) images of SW480 cells treated with fedratinib for 24 hr (Scale bar: 500 nm). White arrows indicate an example of SPLICS$^+$ area. (**C**) Segmentation of organelle membranes of SW480 cells treated with fedratinib for 24 hr (M: mitochondria, ER: endoplasmic reticulum, EL: endolysosome, G: golgi apparatus; Scale bar: 500 nm). Red rectangle highlights area with cristae collapse. (**D**) Principal component analysis (PCA) of metabolomic analysis of cells treated with vehicle or fedratinib for 24 hr. (**E**) Lipidomics analysis and volcano plot from isolated mitochondria from SW480 cells treated with vehicle or fedratinib for 24 hr. (**F**) Confocal images and (**G**) line intensity profile of representative SPLICS$^+$ and SPLICS$^-$ mitochondria of mitochondria membrane potential (MitoTracker Deep Red (MTDR)) and total mitochondrial mass (mitoTagRFP) in cells treated with fedratinib for 24 hr. (**H**) Ratio metric analyses of mitochondria membrane potential from SPLICS$^+$ and SPLICS$^-$ mitochondria in cells treated with fedratinib for 24 hr (n = 16; Scale bar: 1 μm). (**I**) Mitochondria flow cytometry performed on whole cell (n = 10,000) or isolated mitochondrial (n = 100,000) fraction from cells treated with vehicle or fedratinib for 24 hr. $\log_{10}$-scaled MTDR mean fluorescence intensity (MFI) displayed on x-axis and count on the y-axis. Two-tailed paired t-test were performed on (E). **$P \leq 0.01$, ***$P \leq 0.001$.

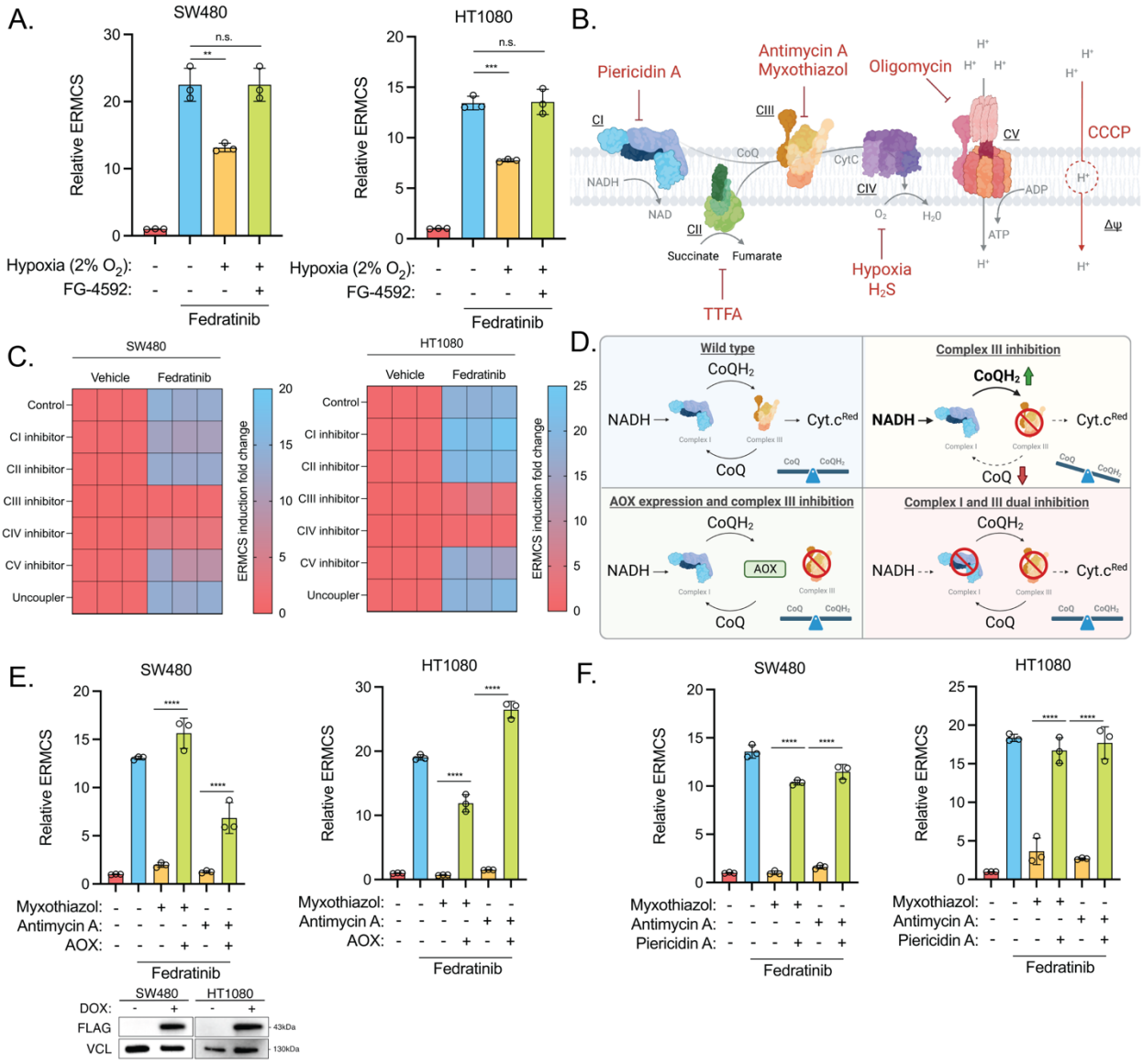

Fig. 4. ETC Complex III function is necessary for ERMCS formation.
(**A**) Relative ERMCS (right) in cells incubated in hypoxia (2% O_2) or treated with a PHD inhibitor FG-4592 (50 μM) for 48 hr, and then treated with fedratinib for 24 hr. (**B**) Diagram of mitochondria electron transport chain (ETC) and specific mitochondrial complex inhibitors (CI: piericidin A (20 nM), CII: TTFA (100 μM), CIII (antimycin A: 100 nM, myxothiazol: 50 nM), CIV (Hypoxia: 2% O_2, H_2S: 250 ppm)). (**C**) Relative ERMCS (right) in cells treated with specific ETC inhibitors for 24 hrs, and then treated with vehicle or fedratinib for 24 hr. (**D**) Diagram illustrating the regulation of CoQ redox state following complex III inhibition, expression of alternative oxidase (AOX) under complex III inhibition, and complex I/III dual inhibition. (**E**) Relative ERMCS in AOX expressed cell treated with complex III inhibition with myxothiazol (50 nM) or antimycin A (100 nM) for 24 hr, and then treated with vehicle or fedratinib for 24 hr. AOX expression was validated with immunoblotting (below). (**F**) Relative ERMCS in cells treated with complex I and III inhibitors Piericidin A (20 nM) and myxothiazol (50 nM), or antimycin A (100 nM) for 24 hr, and then treated with vehicle or fedratinib for 24 hr. For ERMCS measurement with flow cytometry (**A**, **C**, **E, F**), 3 independent experiments were performed. Significance was

calculated with an unpaired two-tailed t-test. n.s. = not significant, **P ≤ 0.01, ***P ≤ 0.001, ****P ≤ 0.0001. Data are mean ± SD.

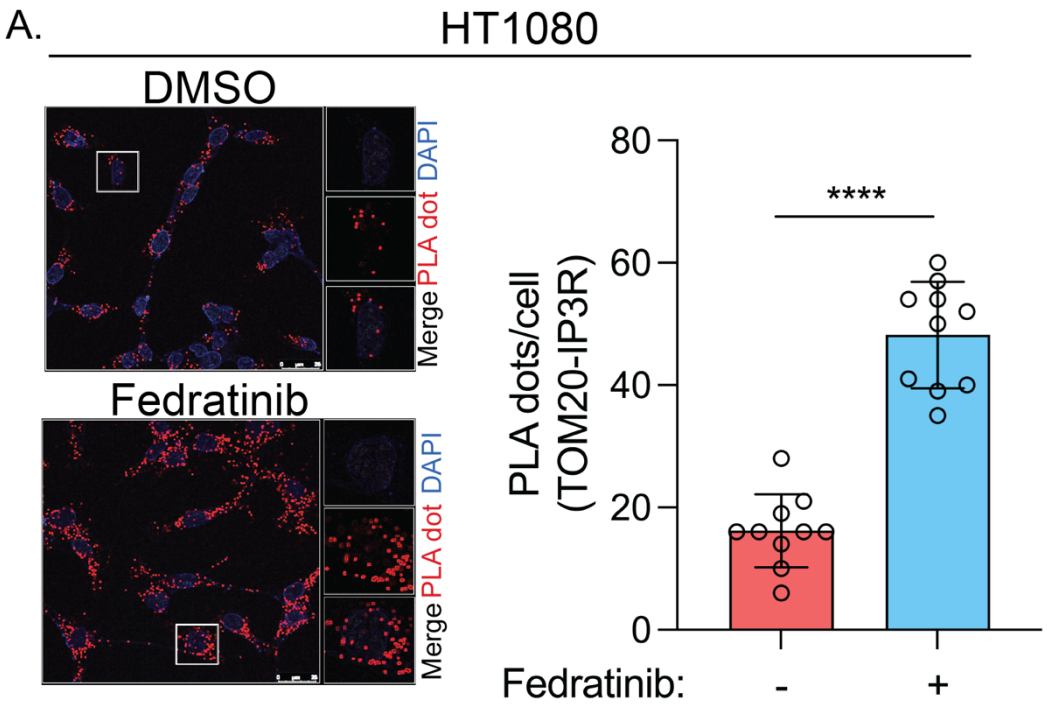

Extended Data Figure 1. Proximity ligation assay validation of Fedratinib induced ERMCS formation.

A. Representative images of PLA experiment in HT1080 cells treated with vehicle or fedratinib for 24 hr. Anti-TOM20 and Anti-IP3R were used as primary antibodies in the assay (Left). Quantification of average number of PLA foci per cell (Right). 10 cells were quantified per condition per independent experiment. n = 3. n.s. = not significant, *P ≤ 0.05, **P ≤ 0.01, ***P ≤ 0.001, ****P ≤ 0.0001. Data are mean ± SD.

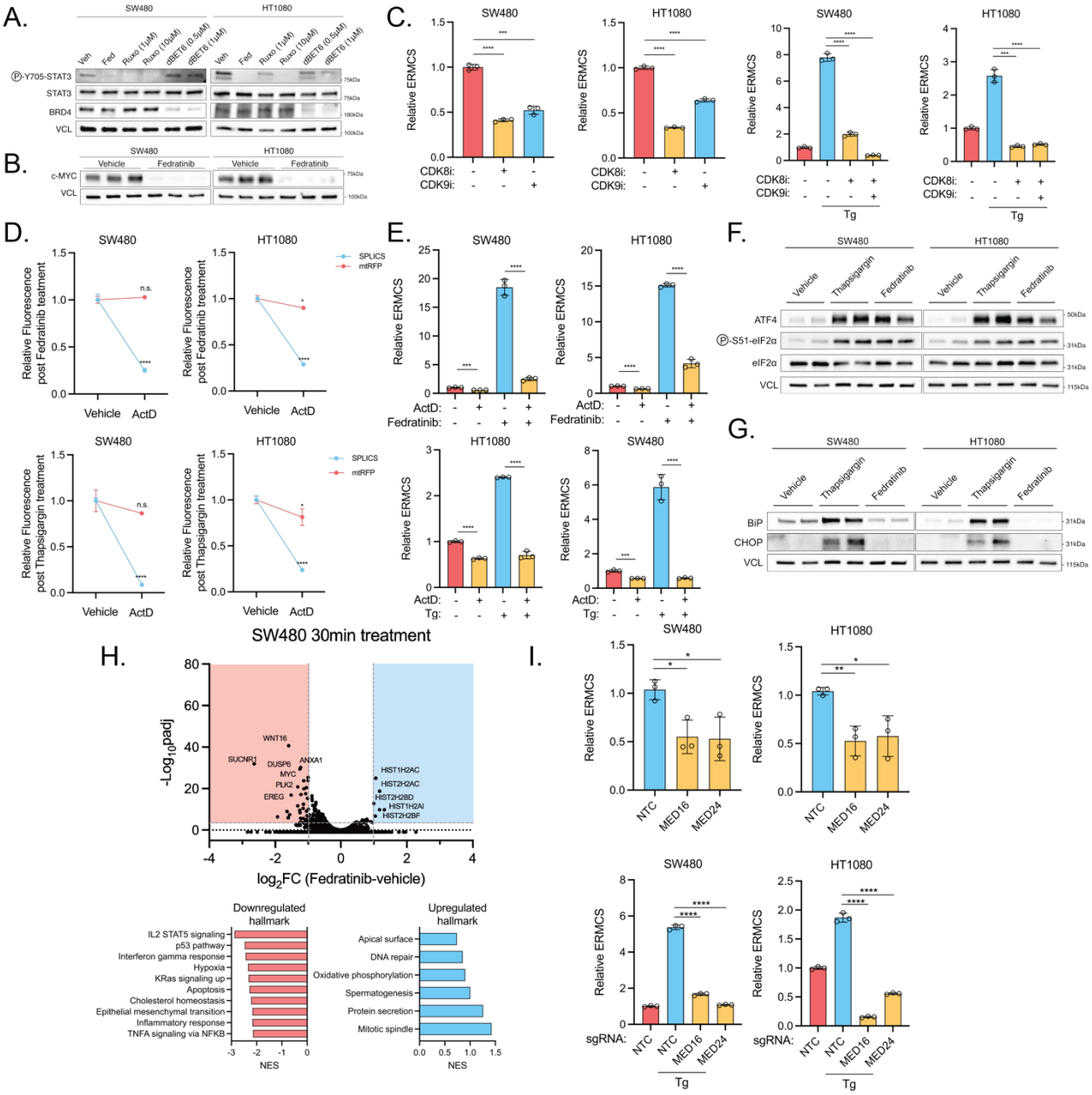

Extended Data Figure 2. Transcriptional regulation of ERMCS.
(**A and B**) Immunoblot from cells treated with vehicle, fedratinib (Fed), ruxolitinib (Ruxo), or dBET6 for 24 hr. (**C**) Relative ERMCS in cells treated with inhibitors of transcription kinase CDK8 (AS-2863619, 1 μM) or CDK9 (NVP2, 1 μM) for 6 hr, and then treated with vehicle or thapsigargin (50 nM) for 24 hr. (**D**) Actinomycin D (10 μg/ml) pulse chase of mitoTagRFP and SPLICS fluorescence after vehicle, fedratinib, or thapsigargin (50nM) treatment. (**E**) Relative ERMCS fluorescence from cells treated with actimonycin D (10 μg/ml) for 24 hr, and then treated with vehicle, fedratinib, or thapsigargin (50 nM) for 24 hr. (**F**) Immnoblot analyses of ER stress markers BiP/HSPA5 and CHOP/DDIT3 from cells treated with vehicle, fedratinib, or thapsigargin (50 nM) for 24 hours. (**G**) Immunoblot analyses of ISR marker ATF4 and phosphorylation of eIF2α^{S51} from cells treated with vehicle, fedratinib (Conc) or thapsigargin (50 nM) for 24 hours. (**H**) Volcano plot of BrU-seq analysis after SW480 cells treated with fedratinib for 30 min (top panel). Normalized enrichment score (NES) of top pathways altered (bottom

panel). (**I**) Relative ERMCS and gene expression level of MED16 and MED24 mRNA transcripts upon CRISPRi mediated knockdown of cells treated with vehicle or thapsigargin (50 nM) for 24 hr. For ERMCS measurement with flow cytometry (**C**, **D**, **E**, **I**), 3 independent experiments were performed. Significance was calculated with an unpaired two-tailed t-test. n.s. = not significant, *P ≤ 0.05, **P ≤ 0.01, ***P ≤ 0.001, ****P ≤ 0.0001. Data are mean ± SD.

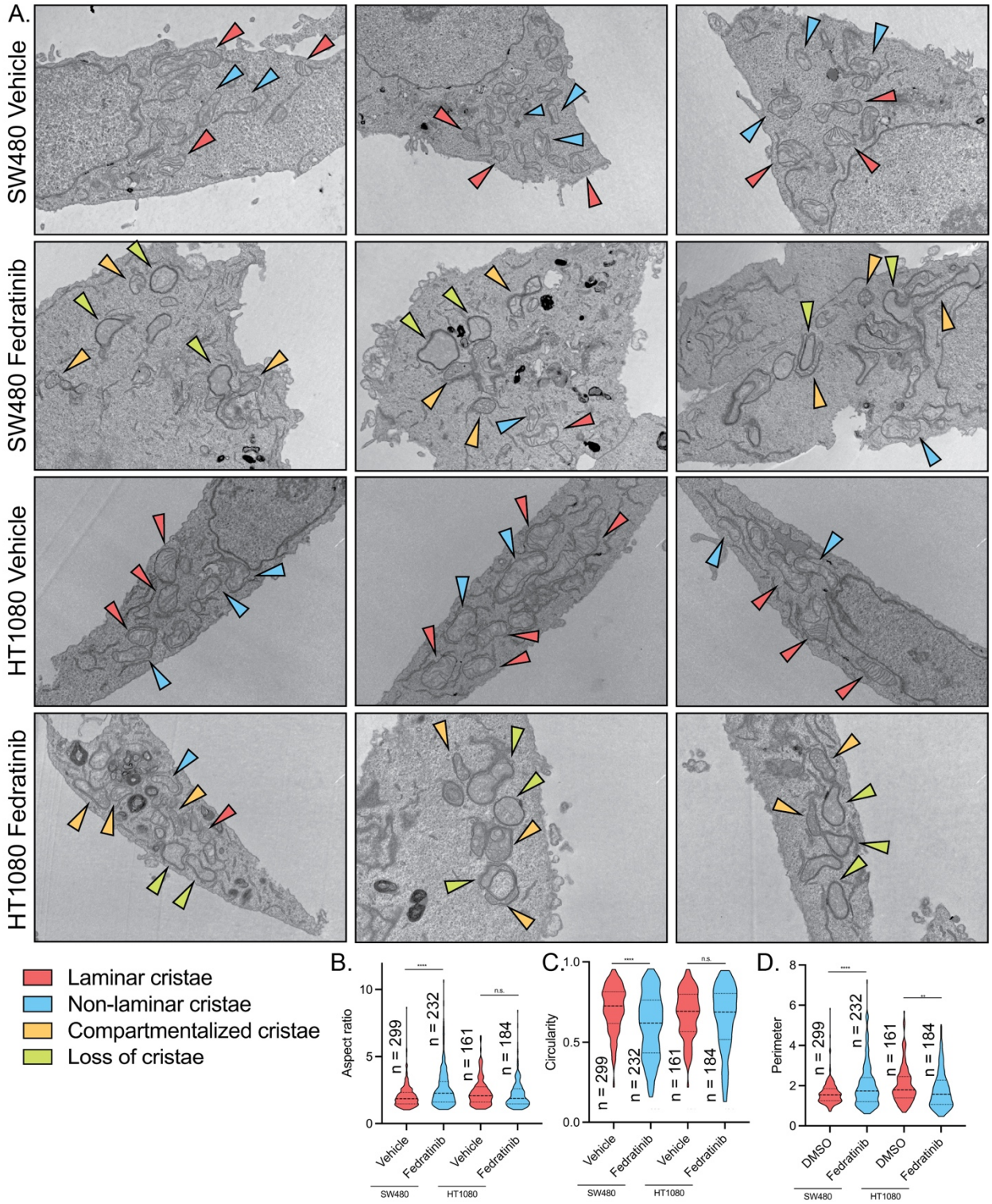

Extended Data Figure 3. TEM analyses of mitochondria in fedratinib treated cells. (**A**) Three representative images in cells treated with vehicle or fedratinib for 24 hr. Cristae structures are annotated in corresponding colors. Red: Laminar cristae. Blue: Non-laminar cristae. Yellow: Compartmentalized cristae. Green: Loss of cristae. (**B**, **C**, **D**) Aspect ratio, circularity, and perimeter (μm) of mitochondria in cells treated with vehicle or fedratinib for 24 hr

(n=161-299). Data are median ± interquartile range (**B**-**D**). n.s. = not significant, **P ≤ 0.01, ***P ≤ 0.001, ****P ≤ 0.0001.

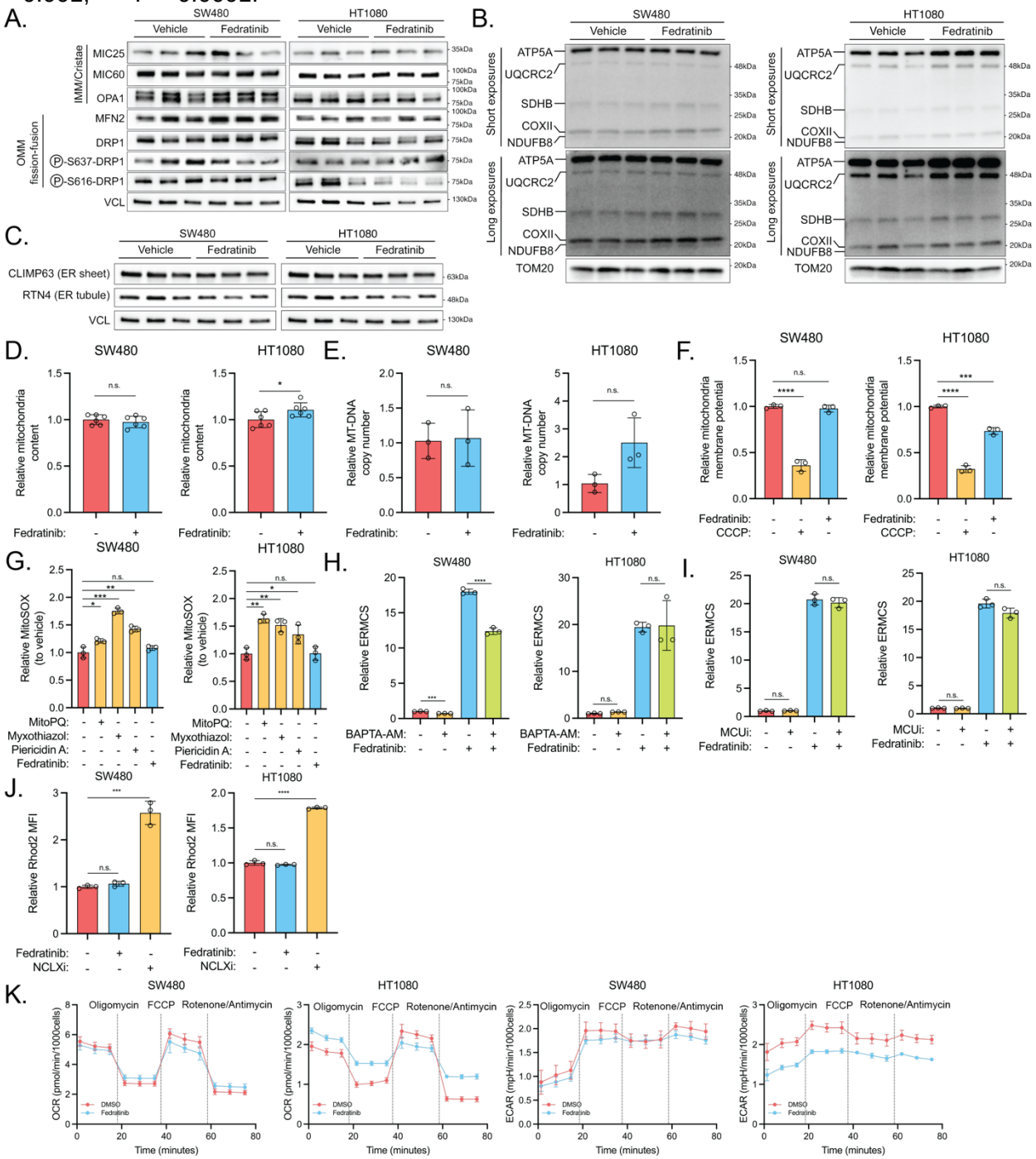

Extended Data Figure 4. Fedratinib does alter various mitochondrial function at the whole cell level.

(**A**) Immunoblot analyses of mitochondrial fusion (MFN2), fission (DRP1, DRP1^{pS637}, DRP1^{pS616}), mitochondria contact site and cristae organization system (MICOS) components (MIC25/CHCHD6, MIC60/IMMT) from cells treated with vehicle or fedratinib for 24 hr. (**B**) Immnuoblot analyses of mitochondria complex I (NDUFB8), complex II (SDHB), complex III (UQCRC2), complex IV (COXII), and complex V (ATP5A) from cells treated with vehicle and

fedratinib for 24 hr. (**C**) Immnuoblot analyses of ER tubulating (CLIMP63/CKAP4) and sheet-forming (RTN4) from cells treated with vehicle and fedratinib for 24 hr. (**D**) Relative mitochondrial content (**E**) mitochondrial DNA (MT-DNA) copy number, (**F**) mitochondrial membrane potential from cells treated with vehicle and fedratinib for 24 hr (Uncoupler CCCP (1 μM) was used as positive control). (**G**) Mitochondrial ROS (mtROS) was assessed using a ratio of MitoSOX Deep Red-to-MitoTracker Green. mito-paraquat (mitoPQ, 10 μM), myxothiazol (25 nM), and piericidin A (20 nM) were used to induce mtROS. (**H**) Relative ERMCS from cells treated with calcium chelation (BAPTA-AM; 5 μM) and (**I**) MCU inhibition (Ru360; 10 μM) for 24 hr, and then treated with vehicle or fedratinib for 24 hr following. (**J**) Mitochondria calcium was monitored with Rhod2 staining from cells treated with vehicle, positive control NCLX inhibitor, CGP-37157 (50 μM), or fedratinib for 24 hr. (**K**) Representative oxygen consumption (OCR) or extracellular acidification rate (ECAR) in cells treated with vehicle and fedratinib for 24 hr. For immunoblotting (**A**, **B**, **C**), flow cytometry experiments (**D**-**J**), and seahorse experiments (**K)** 3 independent experiments were performed. Significance was calculated with an unpaired two-tailed t-test. n.s. = not significant, *P ≤ 0.05, **P ≤ 0.01, ***P ≤ 0.001, ****P ≤ 0.0001. Data are mean ± SD.

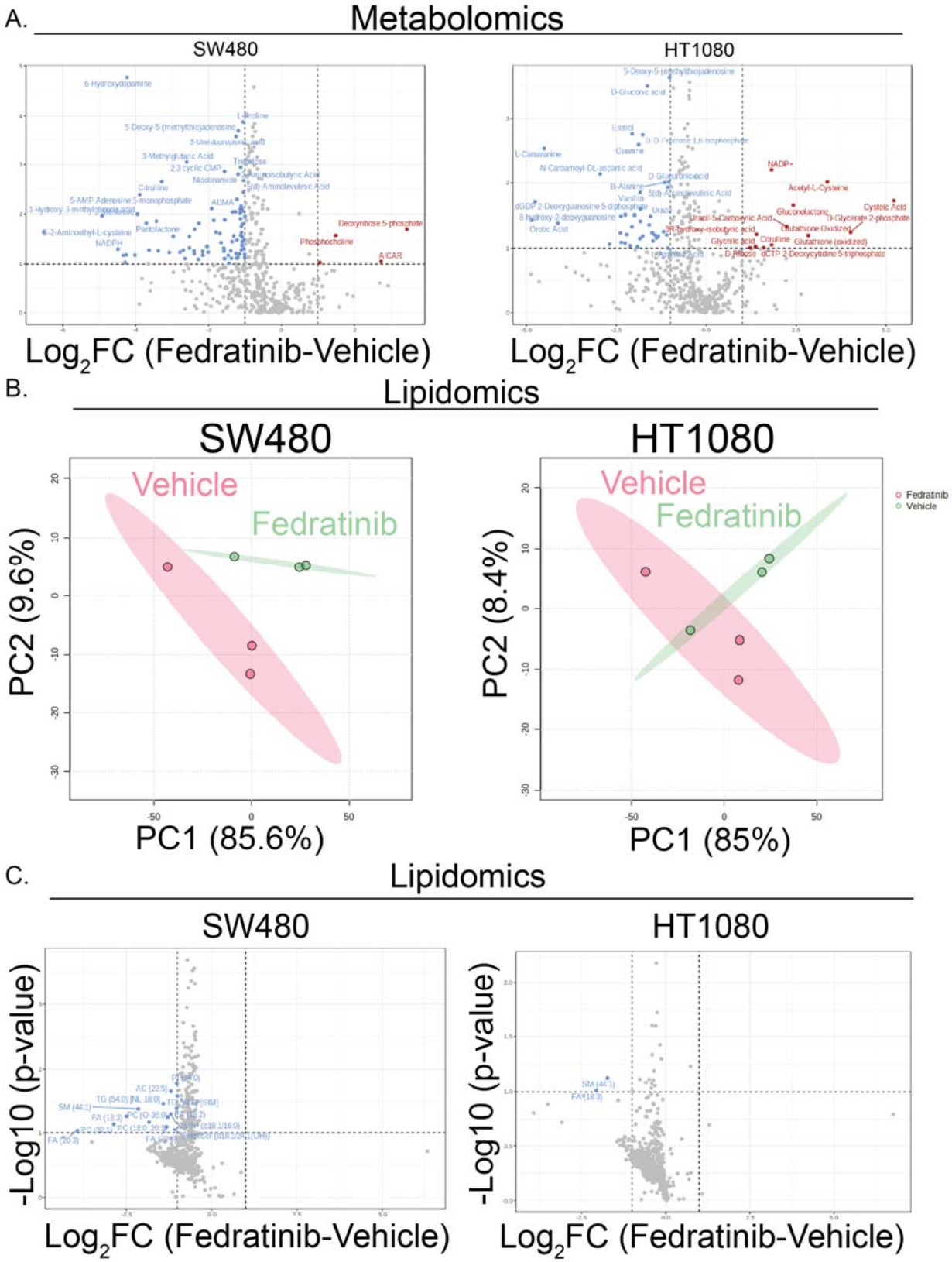

Extended Data Figure 5. Metabolomics and lipidomics analyses of fedratinib treated cells.

(**A**) Volcano plots of polar metabolites in cells treated with vehicle and fedratinib for 24 hr (Log_2(Fold change) is plotted with fedratinib-over-vehicle control). (**B**) Principal component analysis (PCA) of the lipidome from cells treated with vehicle or fedratinib. (**C**) Volcano plots of non-polar lipids from vehicle or fedratinib treated cells. Log2(FC) is plotted with fedratinib-over-vehicle control.

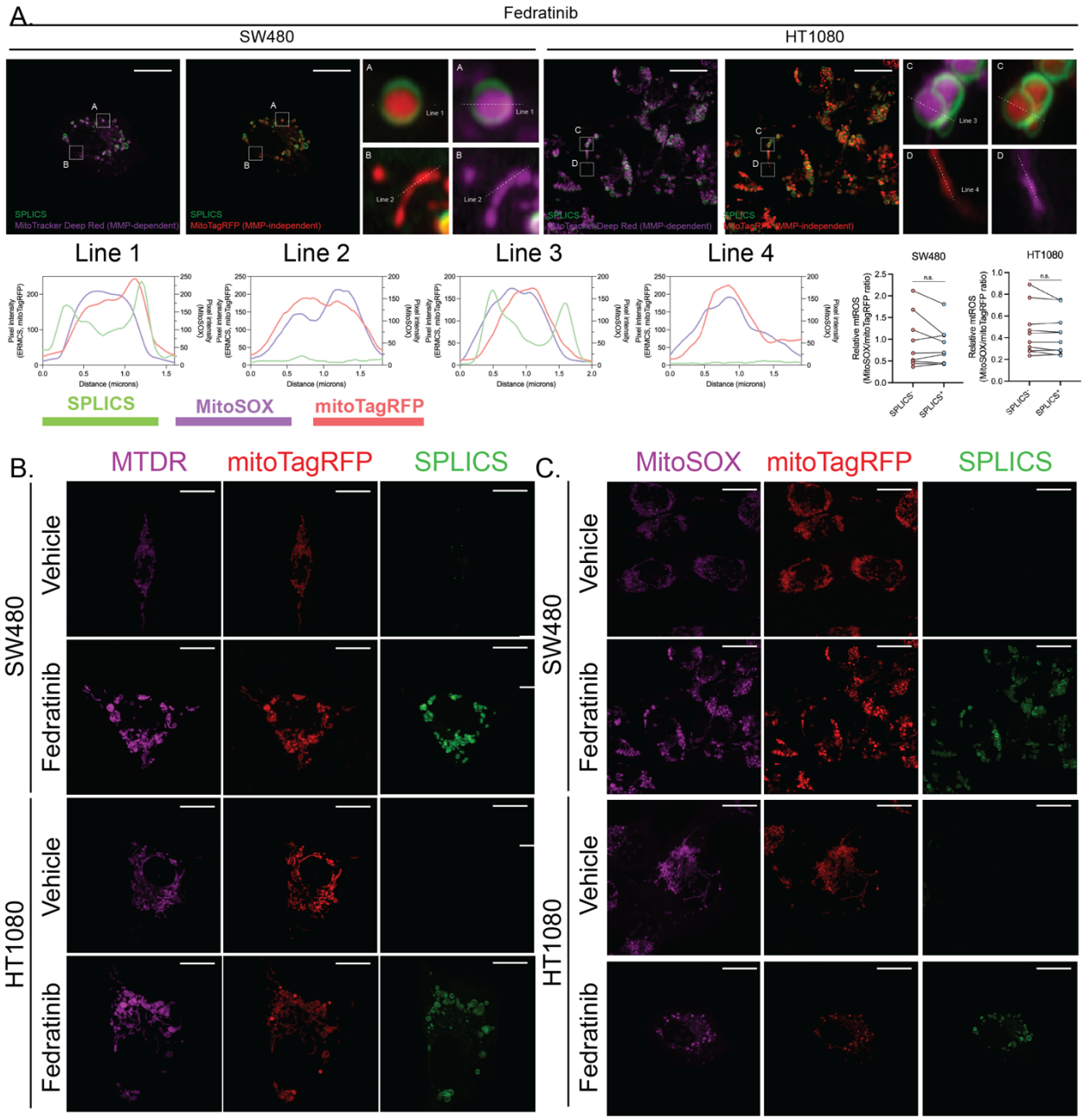

Extended Data Figure 6. Mitochondria reactive oxygen species (mtROS) is not changed in SPLICS^{+} mitochondria.

(**A**) Confocal images of mtROS (MitoSOX Deep Red) and total mitochondrial mass (mitoTagRFP) from cells treated with vehicle and fedratinib for 24 hr (Upper left). Line intensity profile of representative SPLICS^{+} and SPLICS^{-} mitochondria (Lower left). Ratio metic analyses of mitochondria membrane potential via MitoSOX/mitoTagRFP ratio were performed on SPLICS^{+} and SPLICS^{-} mitochondria in cells following treatment with vehicle and fedratinib for 24 hr. Cell number: n = 10 (Right). Scale bar: 1 µm. (**B**) Representative confocal images of MitoTracker Deep Red (MTDR) stained cells treated with vehicle and fedratinib for 24 hr. (**C**) Representative confocal images of MitoSOX Deep Red stained cells treated with vehicle and fedratinib for 24 hr. Two-tailed paired t-test were performed on (A). n.s. = not significant.

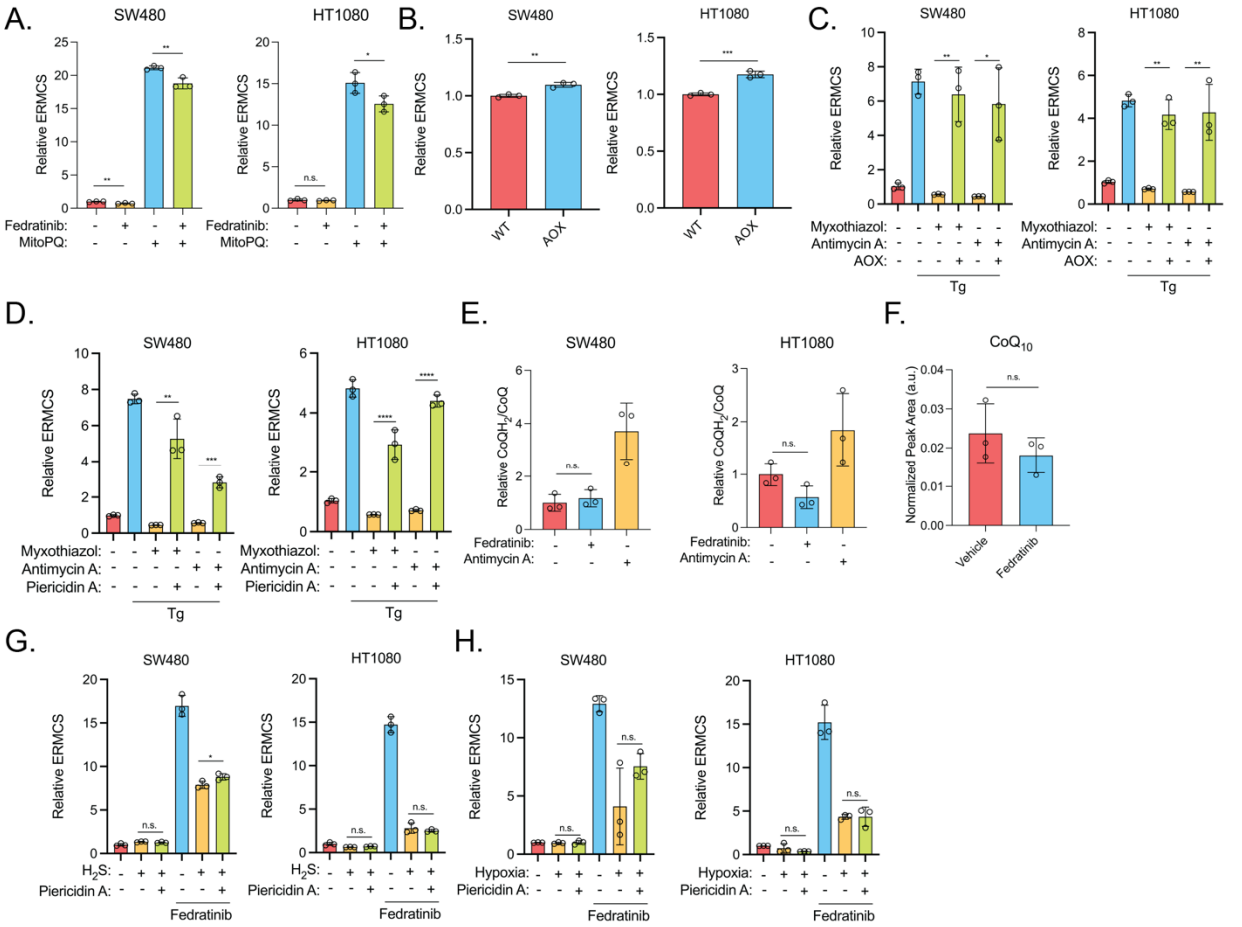

Extended Data Figure 7. Regulation of ERMCS by mitochondrial ROS inducer and modulators of ETC flow.

(**A**) Relative ERMCS in cells treated with mitochondrial-paraquat (mitoPQ, 10 μM) for 24 hr, and then with vehicle or fedratinib for another 24 hr. (**B**) Relative ERMCS in AOX expressing cells. (**C**) Relative ERMCS in AOX expressing cells treated with complex III inhibitor myxothiazol (50 nM) or antimycin A (100 nM) for 24 hr, and then treated with vehicle or thapsigargin (50 nM) for another 24 hr. (**D**) Relative ERMCS in cells treated with complex I and III inhibitor treatment, piericidin A (20 nM), myxothiazol (50 nM), or antimycin A (100 nM) for 24 hr, and then treated with vehicle or thapsigargin (50 nM) for another 24 hr. (**E**) Relative CoQ redox state from cells treated with vehicle, fedratinib, or positive control antimycin A (100 nM) for 24 hr. (**F**) Levels of CoQ_{10} in isolated mitochondria from SW480 cells treated with vehicle or fedratinib for 24 hr. (**G**) Relative ERMCS level in cells co-treated with complex I inhibitor piericidin A (20 nM) and H_2S or **(H)** hypoxia. For ERMCS measurement with flow cytometry (**A**, **B**, **C**, **D**, **G**, **H**,), 3 independent experiments were performed. For mass spectrometry quantification of CoQ species (**E**, **F**), 3 biological replicates were used. Significance was calculated with an unpaired two-tailed t-test. n.s. = not significant, *P ≤ 0.05, **P ≤ 0.01, ***P ≤ 0.001, ****P ≤ 0.0001. Data are mean ± SD.

See accompanying Microsoft Excel document for Supplementary Tables and movies:

Supplementary Table 1. Primary results from image-based drug repurposing screen for ERMSC modulators.

Supplementary Table 2. Raw intensity values for all heatmaps present in the figures.

Supplementary Table 3. BrU-seq data for SW480 cells treated with fedratinib for 30 min and 2 hr.

Supplementary Table 4. CRISPR screening results for regulators of ERMCS.

Supplementary Table 5. Metabolomics and lipidomics values for Fedratinib treated SW480 and HT1080 cells.

Supplementary Table 6. Nucleotide sequences used for primers and oligos.

Supplementary Movie 1: SW480 cells expressing SPLICS and mitoTagRFP being treated with Fedratinib and imaged on Zeiss Lattice Light Sheet 7 for 16 hr. (Available on request)

Supplementary Movie 2: HT1080 cells expressing SPLICS and mitoTagRFP being treated with Fedratinib and imaged on Zeiss Lattice Light Sheet 7 for 16 hr. (Available on request)